COMPUTATIONAL STUDY OF THE DEVELOPMENT OF GRAPHENE BASED DEVICES

A Thesis

by

EDSON PAZUR BELLIDO SOSA

Submitted to the Office of Graduate Studies of
Texas A&M University
in partial fulfillment of the requirements for the degree of

MASTER OF SCIENCE

December 2011

Major Subject: Materials Science and Engineering

Computational Study of the Development of Graphene Based Devices

COMPUTATIONAL STUDY OF THE DEVELOPMENT OF GRAPHENE BASED DEVICES

A Thesis

by

EDSON PAZUR BELLIDO SOSA

Submitted to the Office of Graduate Studies of
Texas A&M University
in partial fulfillment of the requirements for the degree of

MASTER OF SCIENCE

Approved by:

Chair of Committee,	Jorge M. Seminario
Committee Members,	Perla B. Balbuena
	James D. Batteas
Intercollegiate Faculty Chair,	Ibrahim Karaman

December 2011

Major Subject: Materials Science and Engineering

ABSTRACT

Computational Study of the Development of Graphene

Based Devices. (December 2011)

Edson Pazur Bellido Sosa, B.Sc., Universidad Nacional de Ingeniería

Chair of Advisory Committee: Dr. Jorge M. Seminario

Graphene is a promising material for many technological applications. To realize these applications, new fabrication techniques that allow precise control of the physical properties, as well as large scale integration between single devices are needed. In this work, a series of studies are performed in order to develop graphene based devices. First, using MD simulations we study the effects of irradiating graphene with a carbon ion atom at several positions and energies from 0.1 eV to 100 keV. The simulations show four types of processes adsorption, reflection, transmission, and vacancy formation. At energies below 10 eV the dominant process is reflection, between 10 and 100 eV is adsorption, and between 100 eV and 100 keV the dominant process is transmission. Vacancy formation is a low rate process that takes place at energies above 30 eV.

Three types of defects were found: adatom, single vacancy, and 5-8-5 defect formed from a double vacancy defect. Also a bottom-up fabrication method is studied, in this method, the controlled folding of graphene structures, driven by molecular interactions with water nanodroplets, is analyzed considering the interactions with substrates such as SiO_2, HMDS and IPA on SiO_2. When the graphene is supported on

SiO_2, the attraction between graphene and the substrate prevents graphene from folding but if the substrate has HMDS or IPA, the interaction between graphene and the substrate is weak, and depending on the geometry of the graphene structure, folding is possible.

Finally, to evaluate the characteristics of graphene based devices, we model the vibrational bending modes of graphene ribbons with different dimensions. The resonant frequencies of the ribbons and relations between the size of the ribbon and their resonant frequencies are calculated. The interaction of a graphene vibronic device with water and IPA molecules are simulated and demonstrate that this device can be used as a sensitive vibronic molecular sensor that is able to distinguish the chemical nature of the detected molecule. Also, the electrical properties of the graphene vibronic with armchair and zigzag border are calculated; the latter has the potential to generate THz electrical signals as demonstrated in this work.

DEDICATION

To my beloved parents and sister, Amador, Tula and Yemid, for all your love, understanding, guidance and unconditional support. You are my source of inspiration and strength, without you nothing of this would be possible, I love you!

Translation:

A mis amados padres y hermana, Amador, Tula y Yemid, por su amor, comprensión, guía y apoyo incondicional. Ustedes son mi fuente de inspiración y fortaleza, sin ustedes nada de esto sería posible, ¡los amo!

ACKNOWLEDGEMENTS

I would like to thank my committee members, Dr. Balbuena and Dr. Batteas, for their time and effort in being members of my committee. Thanks to Dr. Seminario, for his guidance and support throughout the course of this research. Thanks for giving me the opportunity of being part of your research group, where I learned not only technical and scientific knowledge, but I learned how to be a researcher who is productive and is hungry of new knowledge.

Thanks also go to my friends and colleagues at the Molecular Electronics and Nanotechnology group for all the great moments and for all your support not only with research but with personal matters too, working with you has been a wonderful experience. I would like to thank also my nerdy friends, the bio-inspired boy (Alfredo Bobadilla) and the quantum guy (Shiv Akarsh), for all the always interesting discussions and the late night coffee. I have learned a lot from you guys.

Thanks to the Materials Science and Engineering Program Coordinator, Jan Gerston, for all the help and support. To all the great professors at Texas A&M, for their teaching.

We acknowledge financial support from DTRA/ARO project # W91NF-06-1-0231, ARO/DURINT project # W91NF-07-1-0199, and ARO/MURI project # W911NF-11-1-0024.

Finally, thanks to my family, for all the support and best wishes. Thanks for all the wonderful moments and experiences we share. I always have every one of you in my thoughts.

NOMENCLATURE

2D	Two dimensional
3D	Three dimensional
1D	One dimensional
vdW	van der Waals
NEMS	Nano-Electromechanical System
GNR	Graphene Nano-Ribbon
STM	Scanning Tunneling Microscope
CNS	Carbon Nanoscroll
SWCNT	Single-Walled Carbon Nanotube
MWCNT	Multi-Walled Carbon Nanotube
SiO_2	Silicon dioxide
IPA	Isopropyl alcohol
HMDS	Hexamethyldisilazane
MD	Molecular Dynamics
DFT	Density Functional Theory
KS	Kohn-Sham
CM	Continuum Mechanics
HOMO	Highest Occupied Molecular Orbital
LUMO	Lowest Unoccupied Molecular Orbital

TABLE OF CONTENTS

Page

Page

LIST OF FIGURES

Page

Page

LIST OF TABLES

CHAPTER I

INTRODUCTION

1.1. Motivation and goals

Carbon nano-materials have attracted great interest since the discovery of carbon nanotubes in 1991 by Iijima (*1*) due to their unique physical properties (*2*-*7*). Later on, Novoselov *et al.* proposed a simple method to isolate single atomic layers of graphite obtaining a new carbon allotrope called graphene, which is a true two dimensional (2D) material stable at room temperature (*6*). This carbon sheet one atom thick have extraordinary physical properties (*5, 6*), for instance, it has a Young's modulus of 1 TPa (*7*) a very high electron mobility of 200,000 cm^2/Vs (*8*). Graphene is considered a promising material for many technological applications such as high speed transistors with operational frequencies as high as 50 GHz (*9, 10*), transparent electrodes for touch screens (*11*) and graphene-based composites (*12*).

To realize graphene based electronics, we need new fabrication techniques that will allow us precise control of the building blocks and large scale integration between them. Carbon ion bombardment, is a fabrication technique that has already proved can be used to synthesize large-scale high-quality graphene films with controllable thickness (*13*). However, we still need to improve the technique to be able to pattern and modify the graphene film, in order to form the building blocks and the interconnections between them.

This thesis follows the style of *Science*.

In this work, we study the physics of the ion bombardment that provides the parameters to develop a precise method to control the properties of the graphene building blocks by defect formation, and to pattern and fabricate the electrical connections between devices. Other approach complementary to the ion bombardment that is considered in this work, is a bottom-up approach that takes advantage of the van der Waals (vdW) interactions between molecules and graphene sheets (*14*). We study the conditions at which a cluster of molecules can compete with the non-bonded interactions between a graphene sheet and a substrate in which graphene is supported and finally fold the graphene sheet. By this method, is possible to form three dimensional (3D) structures, which could have applications in several areas including nano-electronics.

If the non-bonded interaction between the graphene sheet and a surrounding group of molecules is not strong enough to produce graphene folding, the non-bonded interactions will certainly perturb its stability. This perturbation can be detected by a change in the natural vibrational frequency of the graphene sheet. And we can use the change in frequency to identify the nature of the molecule that creates the perturbation. Therefore, we can fabricate a graphene based molecular sensor with a very high sensitivity by measuring the vibrational frequency of a graphene sheet. This type of graphene based nano-mechanical sensor will have a much higher sensitivity than conventional nano-electromecanical systems (NEMS) made of bulk materials such as silicon (*15*), because the change in frequency will not only be caused by a change in the mass of the resonator, but also by the vdW interactions that are not negligible in small graphene sheets.

The frequencies at which resonators vibrate depend on their size; as the size of the resonator decreases, the natural frequency increases. We may infer that a resonator of graphene nano-ribbons (GNRs) have very high vibrational frequencies (*16*). This high frequency of vibration can be utilized in high frequency generators that could reach the Terahertz range. These Terahertz devices can have several applications in areas such as medical imaging, security, communication and as an analysis tool in chemistry and physics.

1.2. Background and significance

1.2.1. Graphene synthesis by ion bombardment and lithography

There are several methods of graphene synthesis (*5, 11, 17, 18*), one of those recently developed by Garaj *et al.* (*13*) uses ion bombardment to synthesize high quality graphene films with controllable thickness on polycrystalline nickel substrates. In this technique they bombard with 30 keV carbon ions at several dosages a 500 nm film of Ni supported on Si/SiO_2 wafer. After a heat treatment in vacuum at 1000 °C, graphene sheets with several thickness proportional to the bombardment dosage were synthesized.

Raman maps of prepared samples reveal an increase in overall film quality and thickness as the dose increases. With this technique Garaj *et al.* (*13*) obtained with high dosage a better quality of graphene sheets, but also thicker samples. In contrast, for sheets with low dosage the concentration of defects is higher, and single and double layers are easily achieved.

Once the graphene sheets are synthesized, the next step towards the device fabrication is the patterning and modification of the electrical properties of the desire areas depending on the device design. To author's knowledge, up-to-date, there has not been developed a technique to pattern or modify graphene with carbon ion bombardment. Also up-to-date, the highest patterning resolution of graphene is 2.5 nm obtained using scanning tunneling microscope (STM) lithography by Biró *et al.* (*19-21*).

STM offers two main advantages for lithography, the capability of atomic-resolution imaging, and the ability to locally modify the surface of the samples; therefore, the potential to etch patterns. Biró *et al*. combine the STM feature of surface modification with atomic-resolution imaging in order to fabricate almost atomically precise structures. First, atomic-resolution images are taken and then the sample is rotated to set the crystallographic orientation. Finally, the graphene is cut by applying a constant bias potential and simultaneously moving the STM tip with constant velocity. The lithography parameters typically varied between 2.2 to 2.6 V for the bias voltages and between 1.0 to 5.0 nm/s for the tip velocities.

This technique has many features that are required for the manufacturing of large-scale integrated circuits of graphene; however, it lacks an important feature which is high throughput. For this reason, researchers are working to improve the efficiency of this method and also looking for other alternative techniques, such as ion bombardment, in order to make graphene-based electronics feasible in the near future.

1.2.2. Activated folding of graphene

Recent studies of graphene folding have shown that folded areas of graphene show different electronic properties compared to those of graphene (*22, 23*). These folded graphene structures have the potential to form a new family of 3D carbon nano-structures and be used in many applications including electronics (*14, 24*).

One of the most interesting of these new structures is the carbon nanoscroll (CNS), which is a spirally wrapped 2D graphene sheet with a 1D tubular structure resembling that of a multi-walled carbon nanotube (MWCNT), because its electronic properties are intermediate between graphene and carbon nanotubes (*22, 24*). For instance, armchair nanoscrolls are metallic or semimetallic depending on their sizes and those metallic ones have larger density of states at the Fermi level than metallic single-walled nanotubes (SWCNTs). Zigzag nanoscrolls are semiconductors with energy gaps much smaller than corresponding zigzag SWNTs.

Nanoscrolls can be obtained following a simple technique developed by Xie *et al.* (*24*). The first step is to select suitable graphene monolayer supported on Si/SiO_2 samples by optical microscopy or Raman spectroscopy. Once the samples are selected, a droplet of isopropyl alcohol (IPA) solution (IPA/water ~ 1:3) is placed on the graphene monolayer. The edges start to roll up; when the rolling process stops, another droplet of pure IPA solution is added. The scrolling process continued until the whole graphene sheet is rolled up into a CNS.

In order to engineer carbon nano-structures such as the nanoscrolls, we could use the same technique that Xie *et al.* used for the CNS but in a more controllable way, so

we can also create structures such as capsules, sandwiches and others changing the parameters of the folding process. One attempt to find the graphene folding parameters was a computational work made by Patra *et al.* (*14*). They suggested a method to precisely control the fabrication of such carbon nano-structures using water nanodroplets. In their work they tested the activativation and guide folding of graphene flakes of various shapes using water nanodroplets. For example, they folded a graphene structure formed by two rectangular flakes connected by a narrow strip. In their simulations, they positioned a water nanodroplet above the center of the two flakes at 300 K, and after 250 ps both flakes bind with the droplet and bend the connecting bridge to form a sandwich structure. Similarly, a star-shaped graphene nanoribbon with four blades connected to a central flake with a water droplet above the central flake was tested. The droplet binds by vdW interactions with the central flake and induces bending on the four blades and folds into a closed structure with waters filling its interior forming a graphene capsule.

For GNRs Patra *et al.* (*14*) found four different cases depending on the graphene ribbon width and the nanodroplet radius. The four "phases" are called non-folding, sliding, rolling, and zipping. The non-folding phase occurs when the droplet is small compared with the GNR, and it becomes very difficult for the small droplet to induce folding of the wide ribbon. In the case of sliding, the end where the water droplet is positioned starts to fold fast around the droplet forming a knot structure touching the ribbon surface, and starts to slide fast on it. When the nanodroplet is larger than the width of the GNR, the rolling phase is dominant; in this case the ribbon folds around the

spherical droplet into a closed circular cylinder and starts to roll fast on the ribbon surface until it reaches the other end of the ribbon. Finally, the last phase is zipping; in this phase the ribbon folds from the two sides of the droplet and the ribbon starts to "zip" where its two sides touch each other.

In summary, Patra *et al.*(*14*) have demonstrated that non-bonded interactions between water cluster and graphene structures are able to overcome the potential barrier of graphene bending energy and form stable or metastable structures such as sandwiches, capsules, knots, and rings. However, when we consider a graphene nano-structure supported on a substrate, the graphene-substrate interaction increases the potential barrier that needs to be overcome by the Coulombic and/or van der Waals forces between the graphene and the nanodroplet; this new scenario is investigated in this work.

1.2.3. Graphene based NEMS

Nano-electromechanical systems (NEMS) are widely used in diverse fields ranging from quantum measurement to biotechnology (*15, 25-27*). The smaller the NEMS, the more susceptible are its physical properties to perturbation by external influences enhancing its sensitivity; this fact opens the opportunity for applications such as mass spectrometry, quantum motion detection and radiofrequency signal processing. In the past years researchers have developed smaller resonators reaching the ultimate limits of 1D and 2D resonators which are fabricated from carbon nanotubes and graphene respectively.

A characterization of graphene resonators was done by Bunch *et al.* (*16*). They suspended mechanically exfoliated graphene sheets over predefined trenches etched into a SiO_2 surface. The graphene sheets were doubly clamped or cantilever clamped to the SiO_2 surface by vdW attraction and some devices had gold electrodes between the trenches to make electrical contacts. The measurements were performed at room temperature and in vacuum condition; the resonators are actuated by using either optical or electrical modulation.

In the measurements of amplitude versus frequency in the suspended sheets, multiple resonances are observed, and the most prominent one is associated with the fundamental vibrational mode. In the measurements of 33 resonators, with thicknesses ranging from a single atomic layer to sheets 75 nm thick, the frequency f_0 of the fundamental modes varies from 1 to 170 MHz, where the fundamental resonance mode f_0 is given by:

$$f_0 = \left\{ \left[A\left(E/\rho\right)^{1/2} t/L^2 \right]^2 + A^2 0.57 T/\rho L^2 wt \right\}^{1/2} \quad (1)$$

where E is the Young's modulus, ρ is the mass density; T is the tension in the resonator; t, w, and L are the dimensions of the suspended graphene sheet; and the clamping coefficient, A, is 1.03 for doubly clamped beams and 0.162 for cantilevers (*16*). From Eq. 1 we can predict that in the limit of small tension the resonance frequency f_0 scales as t/L^2. Even when a resonator is not being driven, it will still oscillate due to thermal excitation by a root mean square (RMS) amount $x_{th}=(k_BT/k_{eff})^{1/2}$, where $k_{eff}=m_{eff}w_0^2$ is the effective spring constant of the mode (*16*).

Two applications of nanomechanical resonators are ultrasensitive force detection and ultralow mass detection. The high Young's modulus, extremely low mass, and large surface area make these devices ideal for molecular detection. In this work, we study GNR NEMS which, as previously described, are supposed to have a very high sensitivity and very high resonant frequencies due to their small size.

1.2.4. Vibronics

In current electronics the information is encoded in electron currents. The encoding of information requires a large number of electrons to be able to distinguish the signal from the natural noise. In the transmission of this large number of electrons a large amount of power is dissipated. For this reason researchers are looking for new ways to transmit and encode information with low power consumption. One of this new ways to transfer and encode information, described by Seminario *et al.* (*28-30*), is called "vibronics". This technique uses the vibrational states of molecules as information carrier instead of electrons.

In their work, they used a biological molecule (ALA30) for their MD simulations. They introduced an input signal by mechanically moving an atom in one end of the molecule. And the output signals were taken in the middle of the molecule by measuring the change in the bond length. The input is sequence of triangles and squares and was modulated with a sinusoidal signal with a frequency corresponding to the stretching vibrational mode of a carbon-carbon bond. The output signal was demodulated and showed the same input signal with slightly lower amplitude due to

attenuation in the molecular wire. In summary, they proved that information can be transmitted through molecular wires using molecular vibrations with a very low power dissipation (~50 nW) while working at very high frequencies (~20 THz), making this technique a good candidate for future information technology.

1.3. Outline

In this work, we perform a series of studies designed to develop graphene based devices starting from defining and proposing fabrication procedures, following by the study of the specific characteristics of the device, to finally get to the performance testing as shown in Fig. 1:

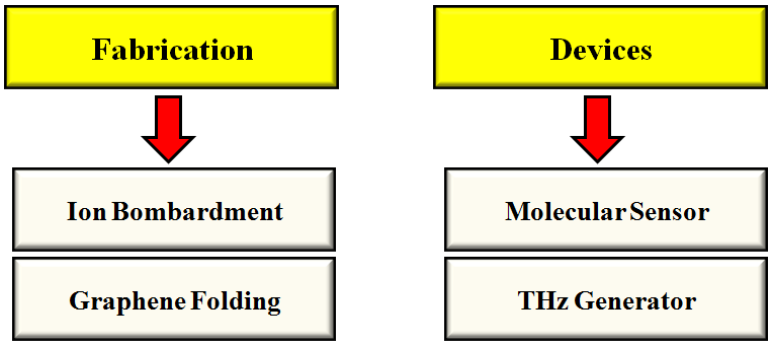

Fig. 1. Scheme showing the outline of the performed research in this work; which is divided in two main parts, fabrication methods and graphene based devices.

A summary of the theory of molecular dynamics, as well as quantum mechanical methods formalism for molecular geometry optimization, and electron transport calculation that we use in this work is described in Chapter II.

In Chapter III, we study using molecular dynamics simulations the effects of bombarding carbon ions on a large graphene sheet. The simulations are carried out at

several ion kinetic energies and at several shooting positions in the graphene sheet considering the symmetry of the 2D hexagonal lattice of graphene. We identify the type of interactions between the carbon ion and the graphene structure, and quantify the rates of occurrence of each type of interaction as a function of ion kinetic energy.

The interaction of graphene sheets supported on silicon dioxide (SiO_2), with water, isopropyl alcohol (IPA), and hexamethyldisilazane (HMDS) molecules is studied in Chapter IV, in order to analyze the non-bonded interactions between graphene and the molecules using molecular dynamics simulations. In this section, we simulate the formation by folding of the graphene sheets that produce scrolls, capsules, rings and sandwiches, which are expected to have different physical properties than those of graphene due to the stretching of the carbon-carbon bonds and the non-bonded interaction between layers.

In Chapter V, we model, using molecular dynamics simulations, the vibrational bending modes of several graphene sheets with different sizes. We calculate the resonant frequencies of the ribbons and find a relation between size of the ribbon and frequency. We also simulate the interaction of graphene ribbons with water and IPA molecules; the interaction of the molecule and the graphene ribbon changes the natural vibrational frequency of the ribbon. This change in frequency can be used to determine the type of molecule present in the system. The graphene ribbons are modeled between two gold electrodes that are used as contacts to calculate the electrical current through the graphene ribbon using a combination of density functional theory and Green function approach. The change in electrical current will depend on the amplitude of the

oscillations and have a frequency proportional to the ribbon vibration which is in the order of Terahertz.

Finally in Chapter VI, we provide the conclusions of this work as well as suggestions for future research.

CHAPTER II

COMPUTATIONAL METHODS

2.1. Molecular dynamics

Molecular dynamics (MD) simulates the physical movements of particles (generally atoms) interacting for a period of time. The trajectories of the particles are determined by Newton's equations of motion, where the potential energy (force field) between the interacting particles in the system determines the force between the atoms and their trajectories.

$$V = \sum_i \sum_{j \neq i} V_{ij} \tag{2}$$

In this work three force fields are used depending on the system to be modeled. To model graphene and carbon structures the widely used three-body Tersoff potential ($V_{ij}^{Tersoff}$) is used, which incorporates the dependence of bond order on the local environment (*31-34*). The Tersoff potential has four terms,

$$V_{ij}^{Tersoff} = f_C(r_{ij})\left[f_R(r_{ij}) + b_{ij} f_A(r_{ij})\right] \tag{3}$$

f_C is a smooth cutoff function to limit the range of the potential and goes from 0 to 1 in a small range D around R.

$$f_C(r) = \begin{cases} 1 & ; \quad r < R - D \\ \frac{1}{2} - \frac{1}{2}\sin\left(\frac{\pi}{2}\frac{r-R}{D}\right); & R - D < r < R + D \\ 0 & ; \quad r > R + D \end{cases} \tag{4}$$

The functions, $f_R(r) = Ae^{-\lambda_1 r}$ and $f_A(r) = -Be^{-\lambda_2 r}$ are repulsive and attractive Morse-like potentials, respectively. The b_{ij} functions are measures of bond order,

$$b_{ij} = \left(1 + \beta^n \zeta_{ij}^n\right)^{-\frac{1}{2n}} \quad (5)$$

and depends of the ζ function

$$\zeta_{ij} = \sum_{k \neq ij} f_C(r_{ik}) g(\theta_{ijk}) e^{-\left[\lambda_3^3 (r_{ij} - r_{ik})^m\right]} \quad (6)$$

where the $g(\theta)$ function is defined as

$$g(\theta) = \gamma_{ijk} \left(1 + \frac{c^2}{d^2} - \frac{c^2}{|d^2 + (cos\theta - h)^2|}\right) \quad (7)$$

where θ represents the angle between bonds *ij* and *ik* and m, γ, λ_3, c, d, h, n and β are chosen parameters to fit the cohesive energy, bulk modulus, and lattice constant of several polytypes of carbon, depending on their coordination number (*33*).

For the case of ion bombardment, we also use the Tersoff potential (*31-34*). However, a short-distance term based on a Ziegler-Biersack-Littmark (ZBL) potential (*35*) is included, which is a screening potential for repulsion at very small interatomic distances. This screening potential becomes important for simulations of particles with very high kinetic energy, as is the case in ion bombardment. The potential energy is as follows:

$$V_{ij} = {}^1/_2 \left[\left(1 - f_F(r_{ij})\right) V_{ij}^{ZBL} + f_F(r_{ij}) V_{ij}{}^{Tersoff}\right] \quad (8)$$

where the f_F term,

$$f_F(r_{ij}) = 1/(1 + e^{-A_F(r_{ij} - r_C)}) \quad (9)$$

is a Fermi-like function that smoothly connects the Tersoff and the ZBL potentials. A_F and r_C are control parameters of the function shape. The ZBL potential has two factors.

$$V_{ij}^{ZBL} = (1/4\pi\varepsilon_0)(Z_i Z_j e^2/r_{ij}) \emptyset(r_{ij}/a) \quad (10)$$

The first factor is the Coulombic potential where Z_i and Z_j are the atomic numbers of the two atoms, e is the electron charge and ε_0 is the permittivity of vacuum. The second term, "∅" is an screening function given by

$$\emptyset(x) = 0.1818e^{-3.2x} + 0.5099e^{-0.9423x} + 0.2802e^{-0.4029x} + 0.02817e^{-0.2016x} \quad (11)$$

with

$$a = 0.8854a_0/Z_i^{0.23} + Z_j^{0.23} \quad (12)$$

where a_0 is the Bohr radius; the a function is only accurate for small separations (less than 1 Å).

To model the folding of supported graphene, and in general to model the molecules involved in this work, we use the CHARMM force field (*36*). This force field has two main components the bonded and non-bonded interactions. For the bonded interactions, we consider bonds,

$$V_{Bond}(r_i) = \frac{1}{2}k_i^b(r_i - r_i^0)^2 \quad (13)$$

where k_i^b and r_i^0 are the bond force constant and bond equilibrium distance respectively. we also consider angles,

$$V_{Angle}(\theta_i) = \frac{1}{2}k_i^\theta(\theta_i - \theta_i^0)^2 \quad (14)$$

where k_i^θ is the angle force constant and θ_i^0 is the equilibrium angle. Finally, the dihedrals or torsions are considered,

$$V_{Dihedral}(\phi_i) = k_i^\phi[1 + cos(n_i\phi_i - \delta_i)] \quad (15)$$

where k_i^{ϕ} is the dihedral force constant and n_i and δ_i are the dihedral multiplicity and phase respectively. For the non-bonded interactions, we consider Lennard-Jones potential,

$$V_{LJ}(r_{i,j}) = 4\epsilon_{i,j}\left[(\sigma_{i,j}/r_{i,j})^{12} - (\sigma_{i,j}/r_{i,j})^{6}\right] \tag{16}$$

where $\epsilon_{i,j} = \sqrt{\epsilon_i \epsilon_j}$ is the minimum value of potential energy and is defined for each pair of atoms, and $\sigma_{i,j} = \frac{1}{2}(\sigma_i + \sigma_j)$ is defined as the zero-crossing distances for the potential. Also Coulombic interactions are considered in the calculations,

$$C(r_{i,j}) = Cq_i q_j / r_{i,j} \tag{17}$$

where q_i is the charge of each atom, C = 1/4πε = 1.44 nmV/e is the Coulomb constant, and ε is the permittivity of vacuum. The non-bonded potentials are affected by a switching function:

$$S(r_{i,j}) = \left[r_{out}^2 - r_{i,j}^2\right]^2\left[r_{out}^2 + 2r_{i,j}^2 - 3r_{in}^2\right]/\left[r_{out}^2 - r_{in}^2\right]^3 \tag{18}$$

This function ramps the energy and force smoothly to zero between an inner (r_{in}) and outer (r_{out}) cutoff. When $r < r_{in}$, Lennard-Jones and Coulombic potentials are not affected by the switching function, and when $r_{in} < r < r_{out}$ all components are affected by the switching function $S(r_{i,j})$.

2.2. Density Functional Theory

Density functional theory (DFT) is a quantum mechanical method used to investigate the electronic structure of many-body systems such as atoms, molecules and

solid state phases. The properties of a system can be predicted by solving the Schrodinger equation:

$$H\Psi = E\psi \tag{19}$$

where Ψ describes the wavefunction of the particles, E is the energy of the molecule and H is the Hamiltonian operator of the system. The full Hamiltonian has two terms the kinetic (T) and potential (V) energy for electrons (e) and for the nuclei (n), and can be written as:

$$H = T + V = T^e(\vec{r}) + T^n(\vec{R}) + V^{n-e}(\vec{r},\vec{R}) + V^e(\vec{r}) + V^n(\vec{R}) \tag{20}$$

The nuclear kinetic energy term (T^n) in Eq. 20 can be neglected using the Born-Oppenheimer approximation (*37, 38*), which considers that the mass of the nuclei is greater than the electron mass and thus moves very slowly with respect to the electrons. The calculation of the complete electronic wavefunction is computationally very intensive. If we consider a system with n electrons, the wavefunction of the molecular system is a function of $3n$ spatial coordinates and n spin coordinates. The Hohenberg-Kohn theorem establishes that all the properties of a molecular system in the ground and excited states are determined by ground-state electron probability density (*39*), which is a function of only 3 variables. This theorem allows calculating the properties of a molecular system by calculating the electron probability density instead of the expensive wavefunction; therefore, DFT allows studying larger molecular systems.

The Kohn-Sham method allows finding the electron probability density without having to find first the wavefunction of the entire system, but the wavefunction of non interacting electrons (*40*). In this method, the electron density of a system of interacting

electrons is represented by the electron density of an equivalent system of non-interactive electrons under an effective potential v_s. Thus, the interacting many-electron problem is split into several non-interacting one-electron problems, which are governed by the Kohn-Sham (KS) equation:

$$\hat{h}^{KS}(r)\theta_i^{KS}(r) = \varepsilon_i^{KS}\theta_i^{KS}(r) \tag{21}$$

where the one-electron KS Hamiltonian h^{KS} is defined as:

$$\hat{h}^{KS}(r) = -{}^{1}/_{2}\,\nabla_r^2 + v_s(r) \tag{22}$$

and the effective external potential is defined as:

$$v_s(r) = -\sum_b \frac{Z_b}{|r-r_b|} + \int \frac{\rho(r\prime)}{|r-r\prime|}dr' + v_{xc} \tag{23}$$

where v_{xc} is the exchange-correlation potential

$$v_{xc}(r) \equiv \delta E_{xc}[\rho(r)]/\delta\rho(r) \tag{24}$$

The external potential (v_s) can be found by solving Eq. 22 self-consistently; the KS molecular orbitals (θ_i^{KS}), shown in Eq. 21, are expanded in terms of the Gaussian-type orbitals.

$$\theta_i^{KS}(r) = \sum_{r=1}^{B} c_{ri}\,\chi_r \tag{25}$$

where B is the number of basis functions of the molecular system, c_{ri} are expansion coefficients of the basis set and χ_r are the functions and that have the general Cartesian form as:

$$\chi_r = cx^n y^m z^l e^{-\alpha r^2} \tag{26}$$

where n, m and l are nonnegative integers, α is a positive orbital exponent, c is a normalization constant, r is the radial coordinate and x, y and z are the Cartesian

coordinates which origin is at the nucleus. Inserting Eq. 25 in Eq. 21 and applying the variational principle, the following equation is obtained:

$$\langle \chi_r | \hat{h}^{KS} | \chi_s \rangle C = \langle \chi_j | \chi_k \rangle E^{KS} C \tag{27}$$

where C is a matrix composed of the expansion coefficients c_{ri}, and E^{KS} is a diagonal matrix composed of all the eigenvalues (energies) of the one-electron KS equation. The expansion coefficients (c_{ri}) of the molecular orbitals are found by solving iteratively Eq. 27 (*41*). The electron probability densities, defined as:

$$\rho = \sum_{i=1}^{n} \left| \theta_i^{KS} \right|^2 \tag{28}$$

and the new KS molecular orbitals, Eq. 25, are obtained during each iterative process until self-consistency is reached. Following the described procedure all the properties of a molecular system can be extracted.

2.3. Electronic transport calculations

To calculate the electronic transport of a system, we use a procedure developed in our group for single molecule transport (*42*). This procedure uses the Hamiltonian matrix obtained from DFT calculations, where for the case of a non-periodic system, few metallic atoms are added to the studied system as part of the contacts. With this the electronic structure and the coupling between the system and the contacts are well described. The Green function for an isolated semi-infinite media is used to model the macroscopic contacts located in the interface. In this approach electrons flow if they can leave one contact, then they get into one of the available electrical channels in the studied system and reach the other contact.

The current will depend on the transmission function $T(E,V)$ and the Fermi-Dirac distribution $f_i(E,V_i)$ in the contacts:

$$I(V) = \frac{2e}{h}\int_{-\infty}^{\infty} T(E,V)[f_1(E,V_1) - f_2(E,V_2)]\,dE \tag{29}$$

The transmission function can be calculated using the Green function:

$$T(E) = Trace(\Gamma_1 G_M \Gamma_2 G_M^{+}) \tag{30}$$

where Γ_i describes the coupling at the contact i, and G_M is the retarded Green function for the studied system including the effect of the contacts and G_M^+ is its adjoint. The Green function G for the whole system in matrix form can be partitioned as follows (*42, 43*):

$$G(E) = \begin{bmatrix} g_1^{-1} & -\tau_1 & 0 \\ -\tau_1^{+} & E - H_C & -\tau_2^{+} \\ 0 & -\tau_2 & g_2^{-1} \end{bmatrix}^{-1} = \begin{bmatrix} G_1 & G_{1M} & G_{12} \\ G_{S1} & G_M & G_{M2} \\ G_{21} & G_{2M} & G_2 \end{bmatrix} \tag{31}$$

where g_i represents the contacts and τ_i describe the coupling between the studied system and the metal of the contacts. H_C is the Hamiltonian of the isolated system and E is the electron energy (*43*). DFT calculations are used to obtain the elements of Eq. 31; Kohn-Sham Hamiltonian (*40*) of a system connected to metal atoms representing the contacts can be partitioned as (*42*):

$$H_{KS} = \begin{bmatrix} H_{11} & H_{1M} & H_{12} \\ H_{M1} & H_{MM} & H_{M2} \\ H_{21} & H_{2M} & H_{22} \end{bmatrix} \tag{32}$$

The subscripts 1 and 2 refer to the contacts and M to the studied system. H_{KS} provides a description of the coupling matrixes and yields valid comparisons among several systems. H_{MM} is assigned to H_C; H_{iM} and H_{Mi} are assigned to τ_i and τ_i^{+}, respectively. The coupling matrixes H_{iM} and H_{Mi} represent the coupling to a geometrically and

electronically perfect continuum. In real situations this may not be case, depending on the system, and the contact may not be perfectly coupled with system. To consider real conditions a coupling factor was introduced as a fitting parameter (*44*) affecting the coupling matrixes. Generally, a coupling factor of 0.5 is adopted (*42*); this indicates that half of the continuum is in direct contact with the extended system. Then we have:

$$G_M[E - H_M] = I \tag{33}$$

where H_M is

$$H_M = H_{MM} - H_{M1}g_1H_{1M} - H_{M2}g_2H_{2M} \tag{34}$$

the g_i for the metallic contact can be approximated as a diagonal matrix with each element proportional to their local density of states (*44*). The coupling between contacts and the studied system is given by:

$$\Gamma_j = i\left[\Sigma_j - \Sigma_j^+\right] \tag{35}$$

where Σ_j is:

$$\Sigma_j = \tau_j^+ g_j \tau_j \tag{36}$$

The chemical potential of the system (μ) is pinned to the Fermi level of the metal contacts when no external field is applied. The Fermi energy for the bulk contact is constant and μ is not used as an adjustable parameter. The applied voltage shifts the Fermi level in the contacts (by E_{f1} and E_{f2}) up and down and μ will relocate in between. This is equivalent to using μ as a reference level and the Fermi levels of the contacts shifting upward and downward accordingly. Both situations are equivalent and do not change the physics of the process, however shifting the Fermi level in the contacts is

preferred for practical reasons; therefore $E_{f1} = \mu - \frac{1}{2}eV$ and $E_{f2} = \mu + \frac{1}{2}eV$ define the energy limits for the calculation of the current (*42*).

CHAPTER III

ION BOMBARDMENT OF GRAPHENE

3.1. Introduction

In most of the graphene applications, control over the electrical and structural properties is required. Functionalization is one way of modifying the band structure of graphene; however, surface functionalization is not easily achieved and generally occurs at the graphene edges (*45*). Other way of tuning the graphene electronic properties is by defect formation (*46*). Defects are intrinsic in graphene production; however, defects can also be created at will by ion bombardment and scanning probe lithography (*47, 48*). Scanning probe lithography techniques can be used to modify graphene structures with high precision, but they are not adequate for mass production. On the other hand, ion beams can be scanned over graphene faster than mechanical tips; and with the advancements in ion beam technology, the spot size can be as small as few nanometers in diameter.

Recently, Garaj *et al.* (*13*) synthesized graphene films with controllable thickness by ion implantation of carbon atoms. Using the same process from the material synthesis to the final device fabrication would be a desire methodology for mass production of graphene devices. The next step for this development is to control the electronic properties by defect formation using carbon atoms for the ion bombardment of graphene.

In this chapter, we simulate using molecular dynamics the bombardment of graphene with carbon atoms in a variety of sites and at several shooting energies. The

physics behind the ion bombardment of graphene with carbon atoms will provide models with their parameters to develop a precise experimental graphene lithography method for controlled defect production that will lead ultimately to graphene integrated device fabrication.

3.2. Methodology

We perform classical MD simulations using the LAMMPS program (*49*). The interaction between atoms is modeled with the Tersoff potential (*31-34*), and includes the short-distance term based on a Ziegler-Biersack-Littmark (ZBL) potential (*35*). Parameters used in the simulations are shown in Table 1.

Table 1. Tersoff-ZBL parameters of the ion bombardment simulations.

Parameter	Value	Parameter	Value
m	3	B	346.7 eV
γ	1	R	1.95 Å
λ_3	0.0 Å^{-1}	D	0.15 Å
c	38049	λ_1	3.4879 Å^{-1}
d	4.3484	A	1393.6 eV
h	-0.57058	Z	6
n	0.72751	r_C	0.95 Å
β	1.5724x10^{-7}	A_F	14
λ_2	2.2119 Å^{-1}		

The modeled system is a 10×10 nm^2 graphene positioned at the origin of coordinates and a carbon atom 3 nm away of the graphene in the *z* axis as shown in Fig. 2. Two ends of the graphene are fixed to simulate a suspended system. The simulations are carried out with a time step of 0.05 fs for energies between 0.1 to 100 eV and 0.01 fs

for energies between 100 eV and 100 keV; the time steps were chosen to assure that there is enough steps during atom interactions occurring within the potential cutoff (2.1 Å). After a minimization, the simulations follow a temperature ramp of with a Berendsen thermostat (*50*) from 10 K to 300 K and a damping time of 100 fs. Then, the systems are kept at 300 K, also with the Berendsen thermostat, with 100 fs damping time, until the systems reach equilibrium, which is when the total energy reaches a steady value. Finally, we set an NVE assembly for the rest of the simulations where the ion bombardment occurs. We imposed a velocity in the –z direction to the carbon atom according to a range of selected energies.

We consider a neutral carbon atom for the bombardment simulations; named hereafter ion despite the fact that the atom has no explicit net charge. We do not consider the charge of the ion because the ion gets neutralized on the surface by charge exchange, considering that the electron movement is at least three orders of magnitude faster than the nuclei. Therefore, we assume that the dynamics of the carbon ion is similar to that of the neutral carbon atom within the Oppenheimer approximation (*37, 38*). Also, considering that in experiments the charge accumulation is prevented by grounding the bombarded sample to ground and the charge each ion carries is neutralized (*51*).

The specified initial position on the ion is the position where the ion hits the graphene, which is chosen to have six symmetric points for each initial position as shown in the inset in Fig. 2, every color represent a group of symmetric points and it will be referred through the text by group name as follows: black ellipses “a”, red squares

"b", pink diamonds "c", blue triangles "d", purple down triangles "e", magenta stars "f" and yellow hexagons "g".

After the MD simulations, the atomic structure of the defects formed by ion bombardment are optimized by DFT, using theB3PW91 hybrid functional (*52, 53*) and the 6-31G(*d*) basis sets (*54*). The calculations have a convergence threshold on the density matrix of 10^{-6} and 10^{-8} for the root mean square and maximum density matrix error between iterations, respectively. The optimizations are followed by a second derivative calculation to determine the existence of a local minimum.

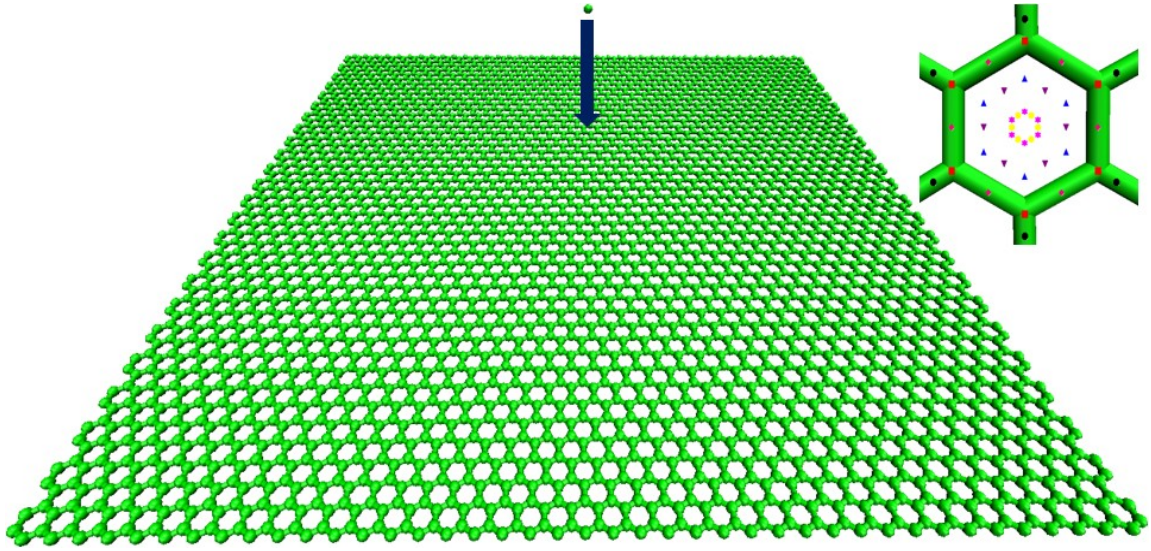

Fig. 2. Simulated system, where a carbon atom hits a suspended graphene sheet. The inset shows the selected positions where the carbon ion hits graphene, the symmetric atoms are color coded: black ellipses (group a), red squares (group b), pink diamonds (group c), blue triangles (group d), purple down triangles (group e), magenta stars (group f) and yellow hexagons (group g).

3.3. Results

The interaction between the ion and the graphene sheet in the bombardment simulations presents four cases: reflection, adsorption, defect formation (damage), and transmission. These types of interactions show a clear dependence on the ion incident energy as shown in Fig. 3. At energies below 1 eV, all the incident ions are reflected. After 1 eV the reflection rate decreases up to 100 eV where none of the ions is reflected anymore. We suggest that the delocalized π electrons over the graphene create an electrostatic repulsion and the incident ion with low energy cannot overcome this repulsion and is reflected. At 1 eV the incident atom has enough energy to overcome the electrostatic repulsion and adsorption of the ion by the graphene surface takes place; the incident carbon atom forms a covalent bond with a nearby atom. At 30 eV the adsorption process becomes dominant. After 100 eV the adsorption rate decreases becoming cero at 10 keV. Defect formation is a low rate process that starts at 100 eV reaching its maximum at 1 keV with a rate of 0.26 and eventually taking a constant rate of 0.14 after 10 keV; during this process two types of defects are created: single vacancy and double vacancy. At high energies the dominant interaction is transmission; its rate increase smoothly between 30 eV to 10 keV where it becomes constant with a value of 0.86.

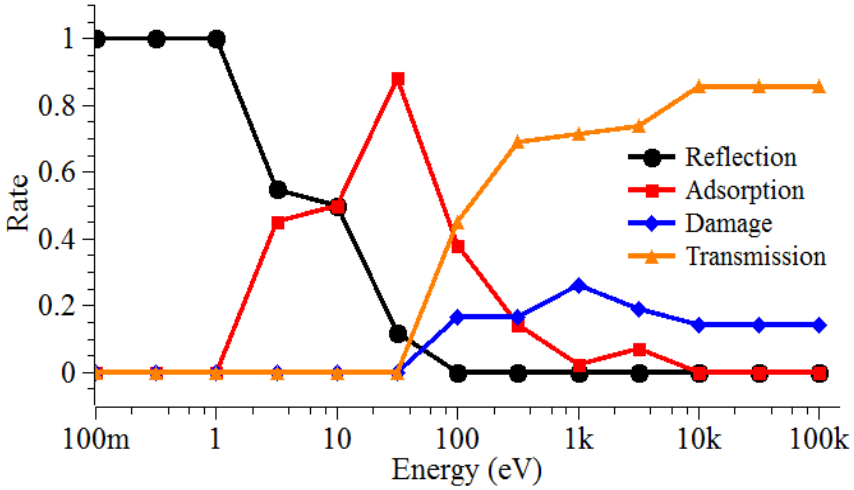

Fig. 3. Rate of occurrence versus kinetic energy of the incident atom for reflection, adsorption, damage, and transmission events.

The type of process has also a dependence of the position where the ion hits the graphene sheet. Considering that the graphene sheet is at 300 K, it is clear that the lattice vibration plays an important role in the simulation results; this can be reflected on the type of event that occurs when we have a group of symmetric points where the ion impacts the graphene. Fig. 4 shows the type of process for each impact position at several energies. As observed, in a group of points not all the positions present the same type of process. Also in Fig. 4, we can observe that at energies below 1 eV the type of event is independent of the position and energy and all the incident ions are reflected. For 10 keV and above, the type of process is independent of the ion kinetic energy and there are two cases depending on the impact position; the ions that hit on top of a carbon atom produce a defect and all the other atoms are transmitted. At intermediate energies, from 3 eV and 3 keV, we have a variety of dynamic processes depending on positions and energies.

At 3 eV, the ions that impact closer to a graphene carbon atom (groups a, b and d) form a bond, this indicate that attractive interaction between carbon atoms contributes to overcome the electrostatic repulsion and promotes bond formation. At 10 eV, the energy of incident ion overcomes the electrostatic repulsion due to the π electrons and there is bond formation; however, when the impact position is closer to a carbon atom the nuclear repulsion due to the direct impact prevents the bond formation and the ion is reflected.

At 30 eV, in most of the impact positions adsorption is the preferred process. For ions in group "a", the nuclear repulsion prevents the formation of a bond and the atom is reflected; however, the reflected ion interacts with neighbor atoms and forms a bond. For group "b" atoms, the preferred event is reflection this suggests that the nuclear repulsion due to the direct impact prevents the bond formation and the ion is reflected. For atoms in group "c", the ion passes through and forms a bond at the back of the graphene. For atoms in groups "d", "e", "f" and "g", there are two cases without dependence of position, the first case is similar than the case of group "c" with bond formation at the back of the graphene, in the second case the incident ion removes a carbon atom and the removed carbon atom forms a bond with a nearby atom.

At 100 eV, some of the ions are transmitted. In groups "f" and "g" all the atoms are transmitted and almost all the atoms are transmitted for group "e". These events suggest that the ions have enough energy to overcome the electrostatic repulsion and that the attractive interaction between atoms is not enough to promote bond formation, and because there is not a collision event, the ions can pass through the graphene sheet. For

atoms in group “d”, there is a strong interaction between ions and carbon atoms. We suggest that the repulsive interaction is nuclear in origin, and due to this repulsion a carbon atom is removed and a defect is formed. In the case of groups “a” and “b” and most of group “c”, there is a different type of process where the incident ion removes one carbon atom and occupies the place of the missing atom (removal/adsorption). For group “a” and “c”, the atomic interaction is similar to the case of group “d” where the nuclear repulsion removes the carbon atom. For group “b”, the interactions is what we consider a direct collision between the ion and the carbon atom. After the removal of the carbon atom the interaction between the incident ion and the neighbor atoms promotes bond formation. Note that for the analysis we consider this process as adsorption since the incident ion is bonded to the graphene structure.

At 300 eV, most of the events are transmission. For groups “c” and “d”, the repulsive interaction with the carbon atoms disturb the graphene lattice in some cases with temporary broken bonds; however, because the time of interaction between the graphene sheet and the ion is smaller than for the case of 100 eV; thus, the ion is finally transmitted in most of the cases. For group “a”, the repulsive interaction is still strong enough to generate a defect. For group “b”, the direct collision produces a removal/adsorption event.

At 1 and 3 keV, most of the atoms are transmitted; however for group “a”, there is still a strong repulsive interaction that promotes defect formation. For group “b”, the direct collision produce removal/adsorption events in some cases and defect formation in others; at this energy we observe the formation of double vacancy defects. Finally, for

10 keV energies and higher, almost all the atoms are transmitted except for group “b” where the direct collision forms single and double vacancy defects.

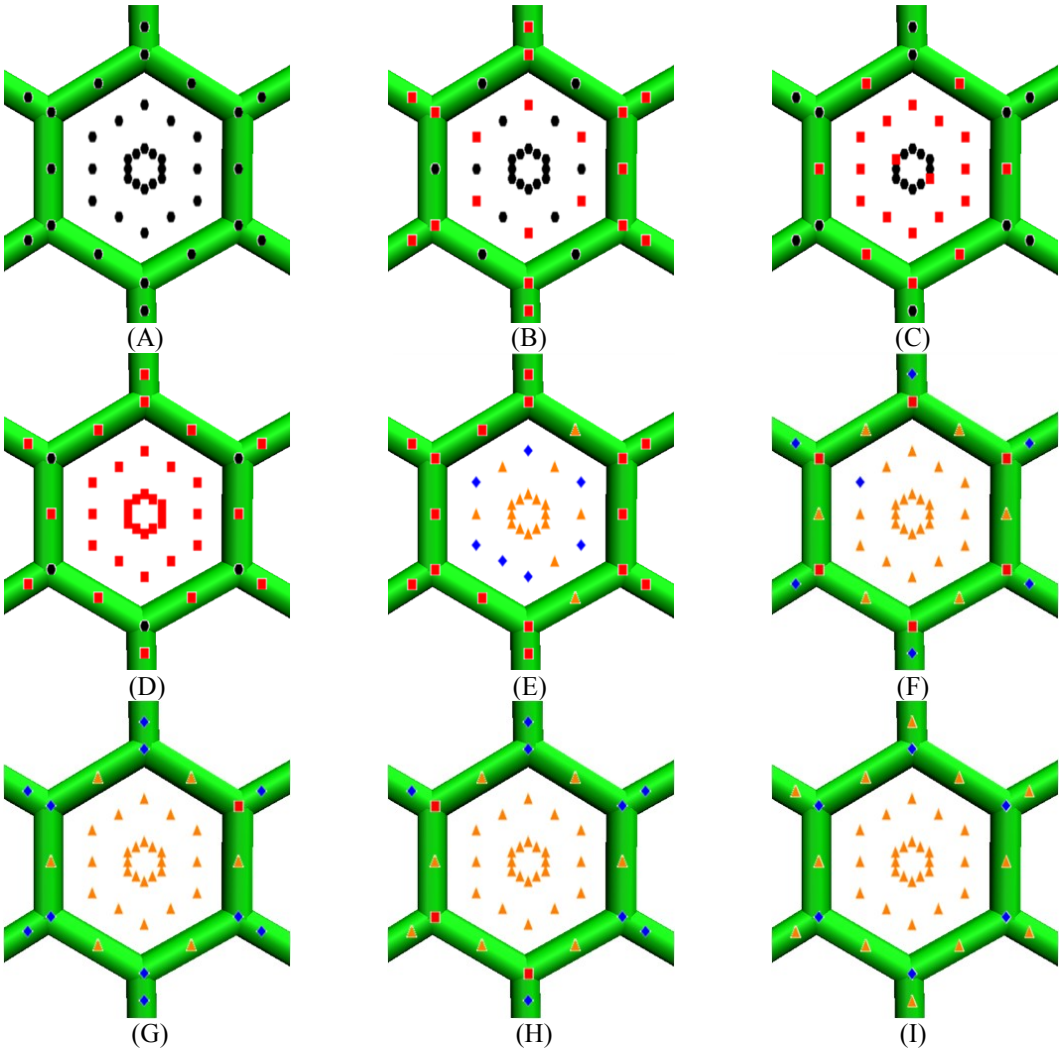

Fig. 4. Impact positions at (**A**) 0.1, 0.3 and 1 eV; (**B**) 3 eV; (**C**) 10 eV; (**D**) 30 eV; (**E**) 100 eV; (**F**) 300 eV; (**G**) 1 keV; (**H**) 3 keV; (**I**) 10, 31 and 100 keV. The type of interaction is color coded: black (reflection), red (adsorption), blue (damage) and orange (transmission).

Other factor to be analyzed in the ion-graphene interactions is the kinetic energies of the ion before and after the interaction with the graphene occurs. The ratio of the incident kinetic energy to energy after the ion interacts with the graphene is a

measurement of the degree of interaction and the amount of energy gained by the graphene structure. Fig. 5 shows the kinetic energy ratio of the ion after reflection, transmission and damage to incident energy. From this curves, we can see that for the case of reflection the interaction between the ion and the graphene is stronger and the ion losses most of its energy, this effect can be attributed to the ion-carbon interaction time, at low energies as is the case of the reflection events the interaction time is long enough to allow local energy equilibration and the graphene gains energy from the ion. For the case of reflection, as the ion energy increases the penetration depth increases, increasing at the same time the atomic attractive interaction, this effect promotes energy exchange especially for hitting positions not close enough to carbon atoms that can produce nuclear repulsion. For the transmission case, we can see in Fig. 5 that as the ion energy increases the energy exchange between graphene and the ion decreases (ion kinetic energy after interaction increases) due to reduction in the ion-carbon interaction time, leaving graphene almost unperturbed at high energies. When a defect is formed, we observe the same trend as in transmission, as the energy increases the energy exchange decreases, and similarly this behavior can be attributed to the interaction time between the ion and carbon atoms in the graphene sheet. The impact position also plays a role, the closer the ion collide with a carbon atom the higher the exchange energy (the lower the ion kinetic energy after interaction).

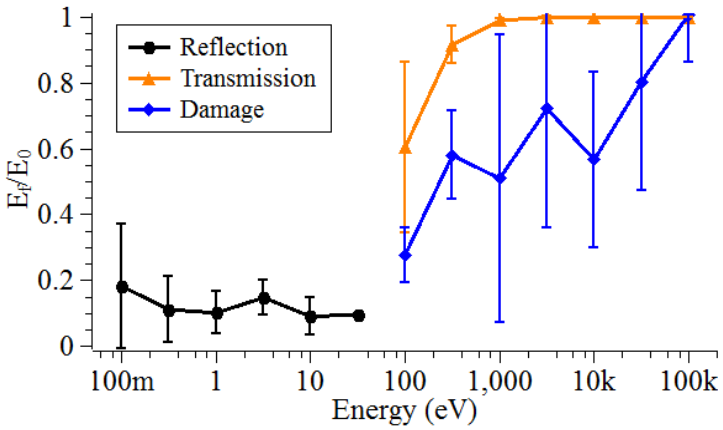

Fig. 5. Kinetic energy ratio of carbon ion after reflection, transmission and damage to incident energy.

In the simulations, we obtain three types of defects one formed by adsorption process and two formed by vacancy formation. After the molecular dynamic simulations, we took the atomic structure of the defects and optimize them using DFT to get a stable structure with a more precise quantum mechanics based method. For the case of adsorption we have two structures from the molecular dynamics simulation; however after the DFT optimization, both structures converge to the same structure as shown in Fig. 6A. This structure called adatom has already been observed experimentally confirming that is a stable defect of graphene in high-vacuum conditions (*55*). To test the stability of the adatom defect in a non-vacuum environment, we optimize the graphene sheet with adatom defect in close proximity of a hydroxyl group and a covalent bond is formed between the carbon atom of the adatom defect and the oxygen atom of the hydroxyl group. Finally, we obtain a functionalized graphene sheet where the reaction is energetically favorable with formation energy of 145 kcal/mol. For the cases where carbon atoms are removed, we have two cases: single and double vacancy formation. In

the single vacancy after the DFT optimization, as shown in Fig. 6B, the distance between two of the carbon atoms closer to the vacancy decreases from 2.63 to 1.69 Å. For double vacancy, we can see in Fig. 6C that the defect is reconstructed after optimization forming two heptagons and one octagon (5-8-5 defect). These two types of defects formed by vacancies have also been observed experimentally (*55*) confirming the accuracy of our calculations.

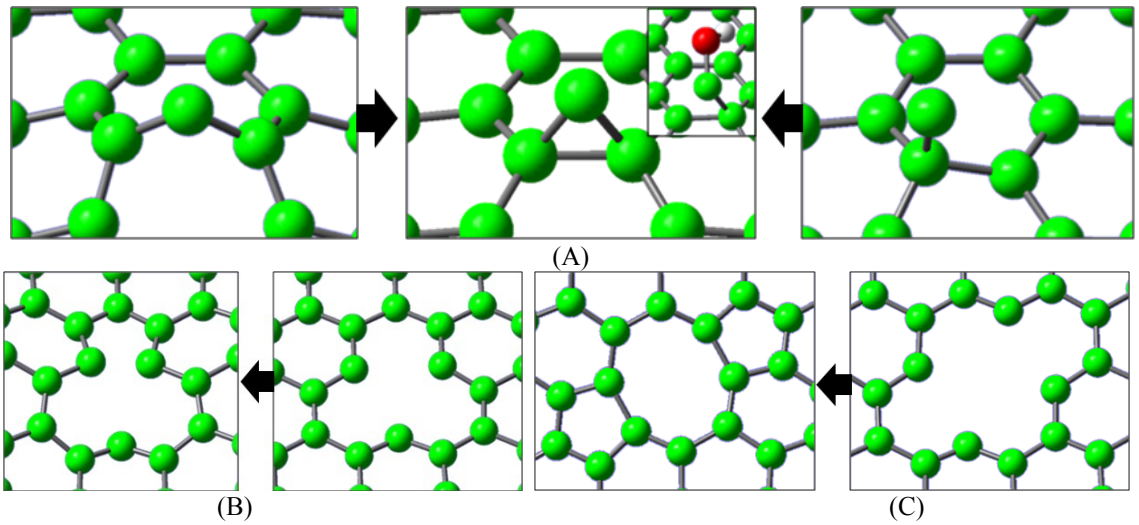

Fig. 6. (**A**) Adatom defect after ab-initio optimization (middle) of MD structures (left and right), the inset figure is a hydroxyl functionalization form from the adatom defect. (**B**) Single vacancy defect and (**C**) double vacancy 5-8-5 defect, after ab-initio optimization (left) of MD structures (right).

To test the formation of structures in the graphene structure by bonding individual atoms, we perform simulations shooting carbon atoms at 20 eV to a graphene sheet. We chose this energy because it is a range where adsorption process is dominant compare with other process, and most of the atoms adsorbed in the graphene are deposited in the front face of the graphene sheet, this facts are helpful in order to build structures on top of the graphene. We simulate two beams one with a diameter of 0.5 nm

and the other with 1 nm. The carbon atoms in the beam are randomly distributed; the use dose for both cases is $4x10^{16}$ ions/cm^2. Every atom in the beam is shot after 20 ps, which is the time it takes for the graphene sheet to reach equilibrium after the impact. We consider this equilibration time because in ion beam experiments the time between impacts is long enough to allow the material to reach equilibrium. Fig. 7A shows the graphene sheet after bombardment with the 0.5nm beam, and Fig. 7B with the 1 nm beam. As we can see for both cases, a carbon structure was formed on top and bonded to the graphene sheet. For the case of the 0.5 nm beam, the structure has an approximate diameter of 1 nm; and for the case of 1 nm beam, the structure has a diameter of 1.5 nm. The bombardment efficiencies of the beam are between 0.6 and 0.7, as predicted in Fig. 3, which means that around 30 to 40% of the atoms in the beam did not formed a bond with the carbon structure. The formed structures are amorphous; however, a more precise analysis of the structures is needed, such as an ab-initio optimization similar to the ones performed for the graphene defects. These ab-initio calculations would be computationally very intensive considering the large number of atoms in the structures. With these simulations, we demonstrate that it is possible building carbon structures on graphene sheets using carbon bombardment, proving that this method is versatile and can be used as a very efficient fabrication process of graphene based devices.

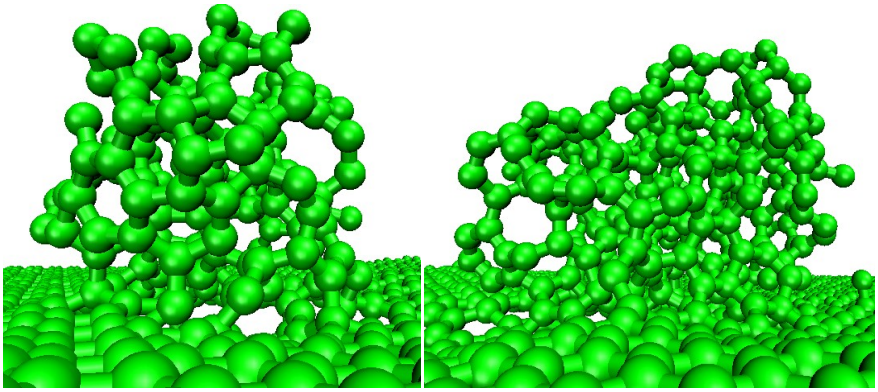

(A) (B)

Fig. 7. Carbon structure formed after bombardment with a (**A**) 0.5 nm and (**B**) 1 nm beam.

3.4. Conclusions

We simulated the carbon ion bombardment of graphene at several energies between 0.1 eV and 100 keV. We observed four types of interactions: reflection, adsorption, transmission and vacancy formation. Reflection is the dominant process at low energies and is principally caused by the repulsive interaction of the carbon ion and the π electrons on the graphene sheet. At energies above 1 eV, the carbon ions have enough energy to overcome the π electrons repulsion and there is an adsorption process, which is the dominant process at between 10 and 100 eV, from the adsorption events adatom defects are formed, the final defect structures were optimized by DFT calculations. Transmission events are observed at energies above 30 eV becoming the dominant interaction after 100 eV. Vacancy formation is observed at energies above 30 eV, and is a low rate process with a constant rate of 0.14 at energies above 10 keV. We obtained single vacancies and double vacancies, from the double vacancies a 5-8-5 defect is obtained after optimization using DFT calculations. We also demonstrate that it is possible to build carbon structures over a graphene sheet by ion bombardment. This

work provide with the analysis and physical parameters to understand the carbon ion bombardment of graphene necessary to develop a lithography method for controlled defect formation that will be a tool in the development of integrated graphene based device fabrication.

CHAPTER IV

FOLDING OF SUPPORTED GRAPHENE*

4.1. Introduction

Recently, a wrapped graphene sheet with a tubular structure (nanoscroll) was fabricated from single graphene sheets with the aid of a solution of IPA and water (*24*). Similarly, other types of carbon nano-structures such as capsules, sandwiches and rings, are expected to acquire some of the properties of both graphene and carbon nanotubes (*24, 56*). Patra *et al.* suggested a method to precisely control the fabrication of such carbon nano-structures using water nanodroplets (*14*). The method relies on the capability of the water cluster to cross the potential barrier of graphene deformation. However, when we consider a graphene sheet on a substrate, the graphene-substrate interaction increases the potential barrier that needs to be overcome by the Coulombic and/or van der Waals forces between the graphene and the nanodroplet. In this chapter, we theoretically analyze the interaction between a nanodroplet and graphene structures supported on substrates such as SiO_2, IPA on SiO_2, and a film of HMDS on SiO_2.

4.2. Methodology

We perform MD simulations with the LAMMPS (*49*) program. The atomic interaction is modeled with the CHARMM (*36*) force field. The force field parameters

* Reprinted with permission from E. P. Bellido, J. M. Seminario, Molecular Dynamics Simulations of Folding of Supported Graphene. *J. Phys. Chem. C* **114**, 22472 (Dec, 2010).

for the molecular structures are adapted from previous works (*14, 57-62*). The Lennard-Jones parameters are shown in Table 2 and the partial charges are shown in Fig. 8. The charges for the graphene structures and for the SiO_2 substrate are calculated by molecular mechanics simulations using MMFF94s force field in Spartan'08, for IPA and HMDS the charges are calculated by DFT calculations using B3PW91 hybrid functional (*52, 53*) and the 6-31G(d) basis sets (*54*), and for water we use the TIP3 model.

Table 2. Lennard-Jones parameters used to simulate the SiO_2 substrate, graphene structures, film of HMDS, water nanodroplet, and IPA. For HMDS the atom type called H-N represents the hydrogen atom bonded to the nitrogen atom (Fig. 8D) and for IPA the atom type called H-O represents the hydrogen bonded to the oxygen atom (Fig. 8B).

Model	Atom type	ϵ (kcal/mol)	σ (Å)
SiO_2	O	-0.152	3.154
	Si	-0.300	3.826
Graphene	C	-0.070	3.550
HMDS	N	-0.200	3.296
	H-N	-0.022	2.352
	Si	-0.300	3.409
	C	-0.110	3.564
	H	-0.022	2.352
H_2O	O	-0.152	3.151
	H	-0.046	0.400
IPA	C	-0.020	4.054
	H	-0.022	2.352
	O	-0.152	3.154
	H-O	-0.046	0.400

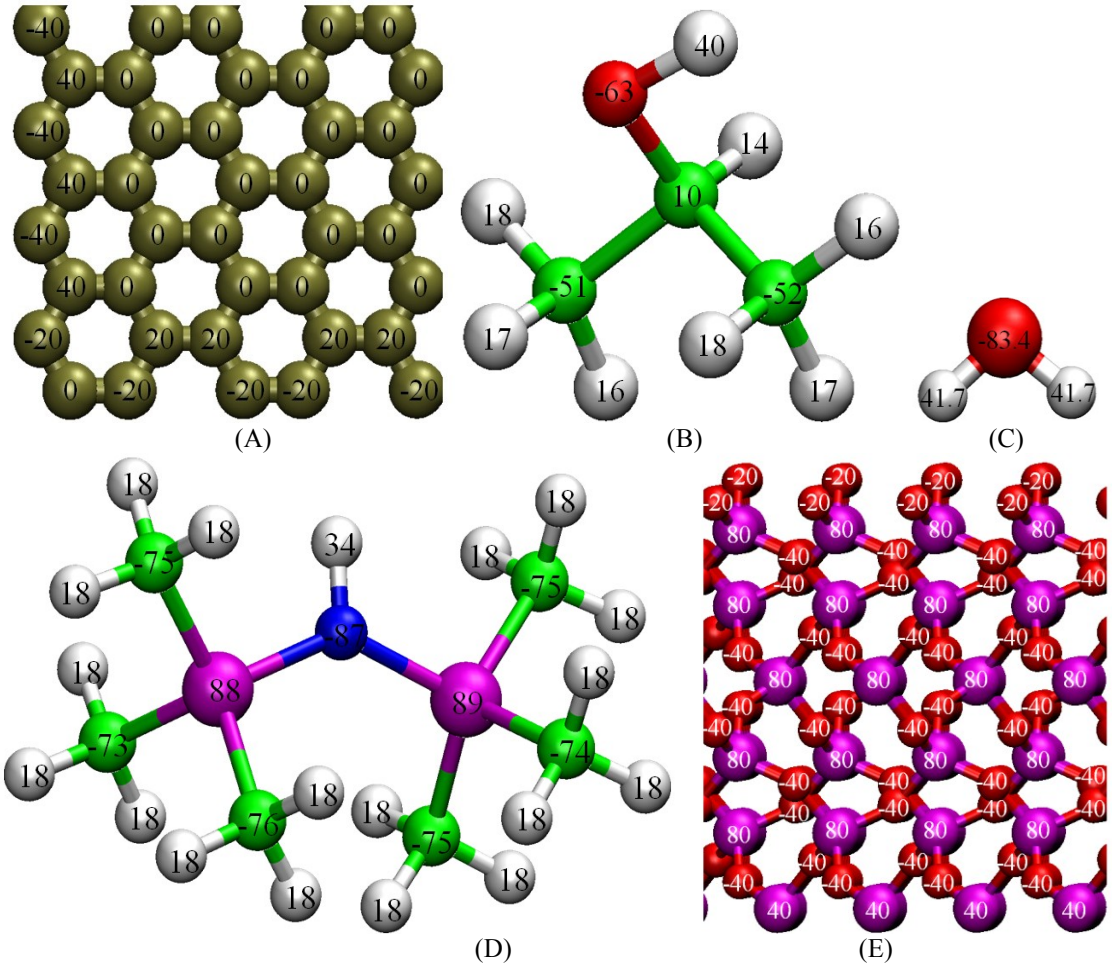

Fig. 8. Partial charges of (**A**) graphene structures, (**B**) IPA, (**C**) water, (**D**) HMDS, and (**E**) SiO_2. All charges are in e/100 units, the atoms are color coded: graphene C (tan), IPA and HMDS C (green), H (white), O (red), N (blue), Si (magenta).

For HMDS, the harmonic parameters for bonds and angles are calculated using the program FUERZA (*60-62*), which is a procedure that takes the Hessian tensor from DFT calculations to calculate the force field parameters. Table 3 shows the bond parameter and Table 4 shows the angle parameters.

Table 3. Bond harmonic parameters used to simulate HMDS.

Bond type	Force constant (kcal/mol)	Bond distance (Å)
H-C	356.28	1.0967
C-Si	169.90	1.8893
Si-N	226.62	1.7517
H-N	493.17	1.0156

Table 4. Angle harmonic parameters used to simulate HMDS.

Angle type	Force constant (kcal/mol)	Angle (degrees)
H-C-H	-44.08	107.6
Si-C-H	-55.29	111.3
C-Si-C	-121.23	109.1
N-Si-C	-122.99	109.8
Si-N-Si	-134.75	133.7
H-N-Si	-42.23	113.0

The input files of the model structures are constructed using Spartan'08, Packmol (*63*), Ampac GUI 9 and homemade software. A 6 x 6 nm^2 flower like structure is constructed with two of the petals with zigzag edges and two with armchair edges; and a nanodroplet (140 water molecules) is positioned at the middle of the graphene structure (Fig. 9). Also a flake structure is constructed with two flakes of 3 x 2 nm^2 connected by a bridge of 2 x 0.7 nm^2; a nanodroplet with 472 water molecules is positioned over the bridge (Fig. 11A). The SiO_2 structure has dimensions of 8 x 8 x 1 nm^3. During the simulations, the base of the SiO_2 is fixed to simulate the bulk structure.

The simulations are carried out with a time step of 1fs and inner and outer cutoffs of 60 Å and 65 Å, respectively. After a minimization, the simulations follow a ramp of temperature with a Nose-Hoover thermostat (*64*) from 10 K to 300 K and a damping time of 100 fs. Then, the systems are kept at 300K with the same damping time, until the systems reach equilibrium. For the flower-like structure, ab-initio calculations are

also performed to get the binding energy of the system; the method and basis set used are Hartree-Fock and 3-21G, respectively.

4.3. Results

We study first the interaction of the flower like graphene structure and a water nanodroplet when the system is isolated and no-substrate interaction is considered (Fig. 9). The system is heated to 300 K, during the heating steps the graphene structure vibrates and begins to get closer to the nanodroplet. At 25 ps, three of the four petals are partially closed, and finally at 50 ps, when the temperature reaches the 300K, the petals are completely closed forming a nano-capsule with the water molecules inside. From 50 ps to 200 ps, the temperature is kept constant at 300 K, the nano-capsule is further stabilized and some water molecules are squeezed away.

To analyze the process of folding, we analyze the non-bonded interactions between the atoms of the graphene-nanodroplet system. During the heating steps (Fig. 9), when the folding process is carried out, the vdW energy decreases; this occurs because the process of the closing of petals of the flower-like structure is driven by vdW attraction between the carbon atoms of the graphene and the water molecules. Therefore, as the petals get closer to the nanodroplet, the vdW energy decreases until all the petals are closed. Between 50 ps and 200 ps, the petals of the nanostructure remain closed; therefore, the vdW energy also remains constant and the Coulombic energy increases between 0 to 50 ps, this occurs because as the petals get closer to the water molecules, the water molecules have less room to move and the Coulombic repulsion increases.

However, between 50 ps to 200 ps, after the nanodroplet is completely inside the graphene structure, some water molecules re-accommodate inside and others are squeezed away of the structure and this translates in a decrease of the Coulombic energy.

The pair energy is defined as the energy of non-bonded interactions, which in our case is the sum of van der Waals energy and Coulombic energy. Despite the fact that the pair energy increases during the closing of petals of the graphene structure, the energy drops as the nano-capsule is stabilized (Fig. 9). To confirm our results, we perform ab-initio calculations of the initial structure and of the completely closed structure. We find out that the binding energy of the initial structure and the completely folded graphene with the nanodroplet inside are -35.9 and -218.2 kcal/mol, respectively. These results suggest that the folding of the graphene structure is driven by a decrease in the graphene-nanodroplet binding energy and confirm that the process is energetically favorable.

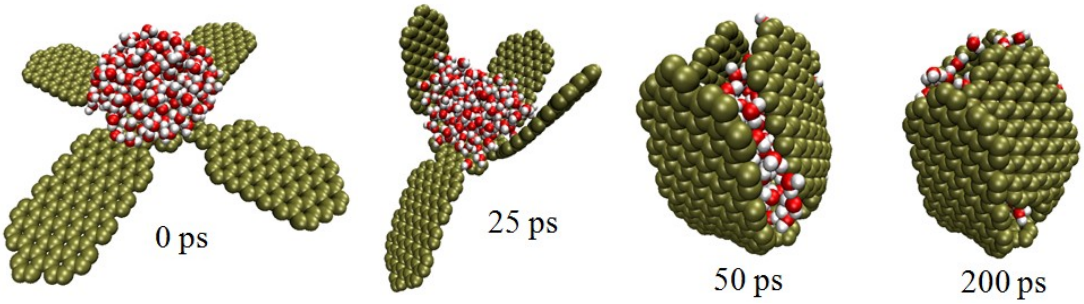

(A)

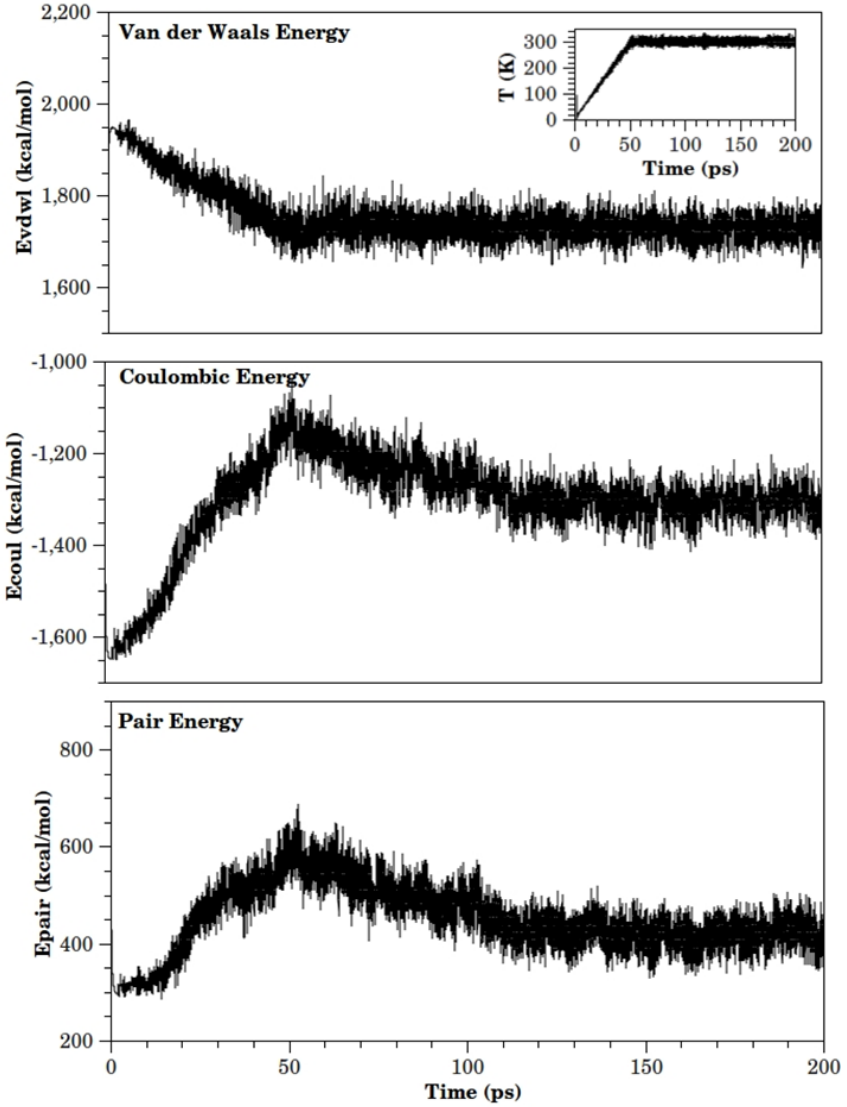

(B)

Fig. 9. (**A**) snapshots of the dynamics of the folding process driven by interactions between the graphene and nano-droplet at 0, 25, 50 and 200 ps, and (**B**) time evolutions of the van der Waals energy, Coulombic energy and pair energy during the molecular dynamics simulation.

When analyzing the graphene flower like-nanodroplet system supported on SiO_2, using the same simulation parameters as in the case of the unsupported structure, the interaction between the graphene and the substrate does not allow the folding process to occur as shown in Fig. 10A. There are three main factors that prevents the folding: the non-bonded interaction between the graphene nanostructure and the substrate is stronger than the interaction between graphene and water molecules. The second factor is that SiO_2 is more hydrophilic than graphene, and for this reason the water nanodroplet expands trying to cover the SiO_2 surface preventing the graphene from folding. And the third factor is that depending on the geometry of the graphene and the water nanodroplet, the contact area between graphene and the substrate is larger than the contact area between graphene and the water nanodroplet.

In order to reduce the SiO_2-graphene interaction, a system with a layer of IPA on top of SiO_2 is used as substrate; the results are similar as the case without IPA (Fig. 10B). The contact area between the graphene flower and the substrate is larger compared to the graphene-nanodroplet contact area preventing the folding. To reduce the attraction between the water nanodroplet and the SiO_2 substrate, a hydrophobic layer of HMDS on top of SiO_2 is also tested: however, as in the previous cases, the folding does not occur (Fig. 10C).

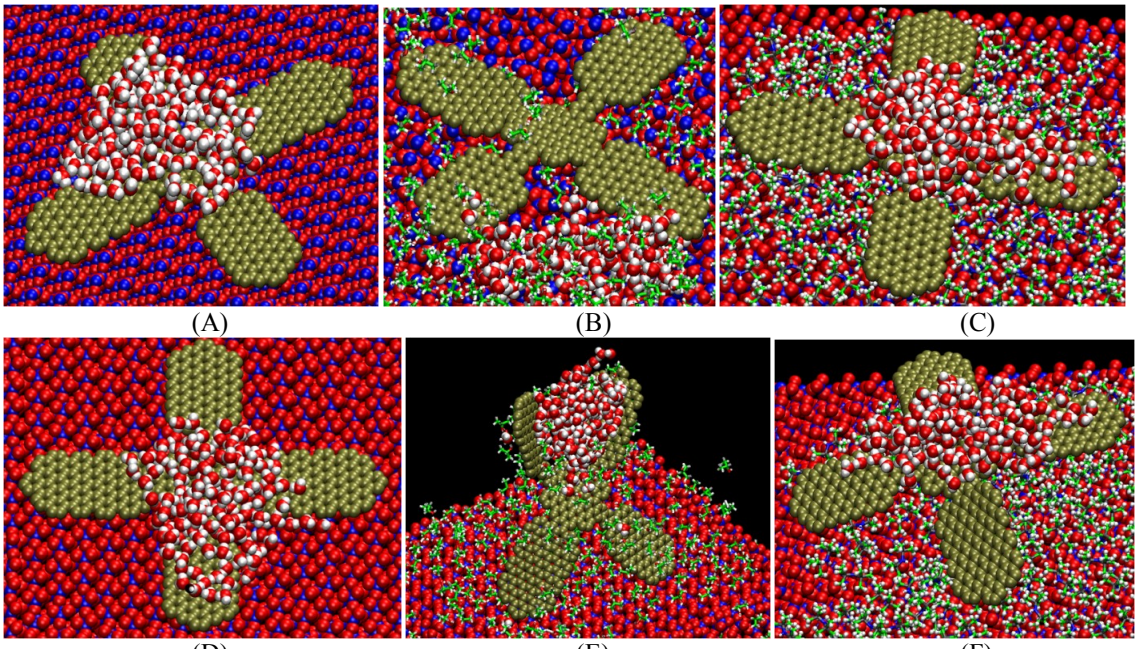

Fig. 10. Interaction of a graphene flower structure with (**A**) a nanodroplet on SiO_2, (**B**) on IPA layer SiO_2 supported, and (**C**) on a HMDS layer SiO_2 supported. Interaction of the defective flower system with (**D**) SiO_2, (**E**) IPA layer supported on SiO_2, and (**F**) HMDS layer supported on SiO_2.

We simulated systems in which we change initial geometry and position the graphene-nanodroplet structure 5 Å away from the substrate (defined as a defective system). This geometry is in agreement with experimental measurements where supported graphene sheets present corrugations with a height depending on the substrate, highs vary from 2 Å to 10 Å (*65-67*), also substrate surfaces are not completely flat and show defects in the scale of some nanometers (*68*). We simulated the defective system supported on a IPA layer on top of SiO_2; since the IPA molecules screen the strong interaction between graphene and SiO_2 and since the initial geometry of the system have reduced the initial contact area between graphene and IPA, the interaction between the water molecules and graphene is not weakened allowing the graphene folding process as seen in Fig. 10E. This result is in agreement with Xie *et al.* experimental results (*24*);

they fabricated CNS using a solution of water and IPA and the initial bending separating graphene from the surface was attributed to surface tension. Finally, we simulate the defective system supported on a layer of HMDS on SiO_2; in this case, the folding is initiated, however the interaction between graphene and HMDS is stronger compared to the water-graphene interaction and the folding does not occur (Fig. 10F).

We also study a flake-nanodroplet system where the flake structure is simulated with the same simulation parameters as the flower structure; the main differences between both structures are that the flake structure has a larger area to interact with its environment and that the water nanodroplet in the flake system is bigger than in the flower system. The first test is the folding of the unsupported flake system (Fig. 11A), where the folding is completed in shorter time compared to the flower structure, which takes place at 25 ps, during the heating steps. The structure is completely folded and stabilizes further during the next heating steps and when the temperature is kept at 300K. The next tests are the simulations of the supported structure on SiO_2, on a layer of IPA supported on SiO_2, and on a layer of HMDS supported on SiO_2; as in the case of the flower-like structure. When the initial geometry is in close contact with the substrate, the folding does not occurs (Fig. 11B-D). This result is expected because the large surface area of the flake structure interacts strongly with the substrate surface and the van der Waals interaction with the water nanodroplet cannot overcome the substrate attraction.

We also perform simulations of the flake-nanodroplet structure positioned 5 Å away of the substrate as in the case of the flower structure for all the previous analyzed substrates. When the defective system is supported on SiO_2 despite the fact that the

folding of the flake structure occurs in shorter time than in the flower system, the interaction with the SiO_2 surface is stronger and does not allow the folding as shown in Fig. 11E. For the defective system supported on a layer of IPA on SiO_2, as in the case of the flower like structure, the folding process occurs (Fig. 11F). Finally, in the defective system supported on a layer of HMDS on SiO_2, the strong van der Waals interaction between the water nanodroplet and the large surface area of the graphene flake overcomes the interaction between graphene and HMDS, allowing the graphene to fold (Fig. 11G). The character hydrophobic of the HMDS does not allow the water nanodroplet to lose the droplet structure favoring the folding process. This last test shows the importance of selecting the adequate geometry of the graphene structure, the correct size of water nanodroplet, and the correct substrate in order to control the graphene folding process.

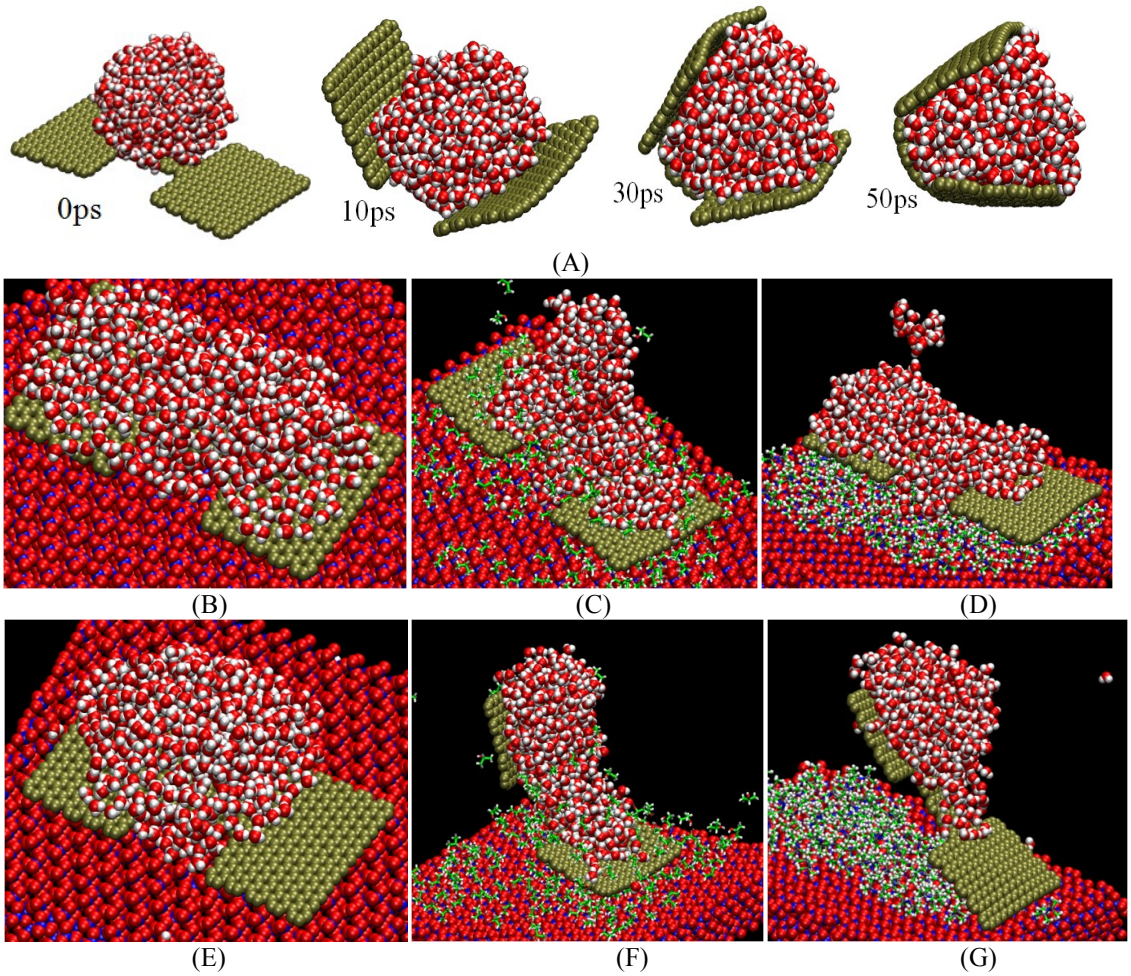

Fig. 11. (**A**) Folding dynamics of the graphene flake structure. Interaction of a graphene flake structure with (**B**) a water nanodroplet on SiO_2, (**C**) IPA layer supported on SiO_2, and (**D**) HMDS layer supported on SiO_2. Interaction of the defective flake system with (**E**) SiO_2, (**F**) IPA layer supported on SiO_2, and (**G**) HMDS layer supported on SiO_2.

4.4. Conclusions

We have studied the folding of a flower like graphene structure and a flake graphene structure driven by the vdW force between the carbon atoms and water molecules. We demonstrate that the non-bonded interactions between a graphene nano-structure and SiO_2 are strong enough to prevent the folding process. We have also demonstrate that the large contact area of a defect free system of graphene supported on

a layer of IPA or HMDS over SiO_2 does not allow the graphene to fold. However, when we have a defective system over a layer of IPA supported on SiO_2, the water-graphene interaction overcomes the graphene-substrate interaction promoting the folding process. Also when we use a hydrophobic substrate such HMDS and the correct graphene geometry with large surface area and adequate nanodroplet size, the folding can occur. In summary, the adequate selection of substrate, graphene geometry, and nanodroplet size allows the folding and may open the possibility of a controlled fabrication of graphene based capsules, scrolls, sandwiches and rings.

CHAPTER V

GRAPHENE VIBRONIC DEVICES

5.1. Introduction

NEMS are devices that are investigated and are ubiquitous in many fields nowadays (*15, 25-27, 69*). Device performance improves as the resonant frequency increases and the NEMS mass decreases, so researchers are working to develop smaller NEMS; however, the ultimate performance of these devices is still yet to be achieved. This ultimate performance can be achieved with the development of 2D and 1D NEMS, which are fabricated from carbon nanotubes and graphene respectively.

A characterization of large graphene resonators was done by Bunch *et al.* (*16*). In their work, they measured amplitude versus frequency in the suspended graphene sheets and observed multiple resonances with the fundamental vibrational mode varying from 1 to 170 MHz. They also found oscillations were present without being externally driven. These oscillations were natural thermal vibrations intrinsic of the graphene sheets.

Also Seminario *et al.* (*28-30*) had demonstrated the use of intrinsic vibrational modes to transport information through molecules. In their method, which forms part of the vibronics scenario because it uses vibrational modes as carrier, the signal is modulated in a terahertz carrier corresponding to an intrinsic resonant frequency of the molecule and is recovered using digital signal processing techniques.

This work studies the natural oscillations of small graphene ribbons that can be utilized in several types of devices such as NEMS, that at very small scales is considered

a vibronic device. These vibronic devices can be utilized as sensors and THz generators, as this work demonstrates, and also have the potential to form devices able to encode, transfer and process information (*28-30*).

5.2. Methodology

To model the graphene vibronic devices and their interaction with other molecules, We perform classical molecular dynamics simulations (MD) using the LAMMPS program (*49*). The graphene structures are modeled using the Tersoff potential (*31-34*) and the parameters used for the graphene devices are listed on Table 5.

Table 5. Tersoff parameters used for the graphene vibronic devices.

Parameter	Value	Parameter	Value
m	3	B	346.7 eV
γ	1	R	1.95 Å
λ_3	0.0 $Å^{-1}$	D	0.15 Å
c	38049	λ_1	3.4879 $Å^{-1}$
d	4.3484	A	1393.6 eV
h	-0.57058	β	1.5724×10^{-7}
n	0.72751	λ_2	2.2119 $Å^{-1}$

For the study of the interaction of the vibronic devices with molecules, we use water and IPA molecules as a test, and these are modeled using the CHARMM force field (*36*). For water, we have that the bond force constant and the equilibrium distance for the oxygen-hydrogen bond is 450 kcal/mol and 0.957 Å respectively; also the angle force constant is 55 kcal/mol and the equilibrium angle is 104.5˚. For IPA, the bonded

parameters are listed in Table 6. The non-bonded parameters for all the molecules are listed in Table 7.

Table 6. Bonded component parameters used to simulate IPA.

Bond Type	Force constant (kcal/mol)	Bond distance (Å)	Angle type	Force constant (kcal/mol)	Angle (°)
C-C	222.5	1.500	C-C-C	53.35	111.5
C-H	309.0	1.111	C-C-H	34.50	110.1
C-O	428.0	1.420	C-C-O	75.70	110.1
O-H	545.0	0.960	C-O-H	57.50	106.0
			H-C-H	35.50	109.0
			H-C-O	45.9	108.9

Table 7. Lennard-Jones parameters used to simulate the graphene vibronic devices and the interacting molecules (water and IPA). For IPA the atom type called H-O represents the hydrogen bonded to the oxygen atom, also the charges for H and C varies depending on the position and can be seen in Fig. 8 (*70*).

Model	Atom type	ϵ (kcal/mol)	σ (Å)	q_i (e^+)
Graphene	C	-0.070	3.550	0.0
H_2O	O	-0.152	3.151	-0.834
	H	-0.046	0.400	0.417
IPA	C	-0.020	4.054	~ -0.3 (*70*)
	H	-0.022	2.352	~ 0.166 (*70*)
	O	-0.152	3.154	-0.627
	H-O	-0.046	0.400	0.399

To construct the input files of the graphene vibronic devices we use Packmol (*63*), Ampac GUI 9 and homemade software. The vibronic devices are small graphene ribbons connected in one end to a larger graphene and free in the other end (Fig. 12). This type of structure can be fabricated by lithography from large graphene sheets, and to date the ribbons can be as small as 2.5 nm wide (*19-21*). In our model, the large graphene sheet in one end is represented by a 1.6 x 15.6 nm^2 graphene structure with a graphene ribbon in the middle. Twenty different graphene structures are modeled where

the size of the ribbons varies as shown in Table 8. The "z" internal coordinate of the atoms are monitored during the simulations and in this way we can calculate the frequency of the bending vibrational modes of each graphene ribbon (Fig. 12). The simulations start with a minimization, followed by a ramp of temperature from 1 K to 300 K. Then, the systems are kept at 300 K for 0.3 ns, the time at which the structures reach equilibrium; once the system is in equilibrium the frequency measurements are carried out for 10 ns. For the test of the interaction between the graphene vibronic devices and water and IPA molecules, we use inner and outer cutoffs of 75 Å and 80 Å, respectively. In the simulations, after the system reach 300 K, 0.5 ns of equilibration time is taken before measuring the frequency for 10 ns. All the MD simulations are carried out with a time step of 1 fs and Berendsen thermostat (*50*) with a damping time of 100 fs.

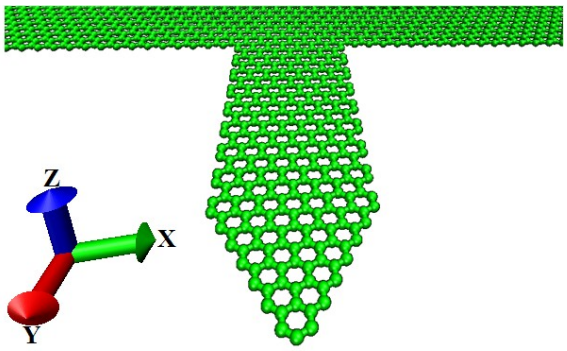

Fig. 12. Model used to simulate a graphene based vibronic device.

To calculate the electrical properties of the graphene vibronic devices, we used the commercial software called Gaussian (*71*), and two models are considered one with armchair border and another with zigzag border, both connected through gold atoms that

represent the electrodes as seen in Fig. 13. The structures are optimized by density functional theory (DFT) using B3PW91 hybrid functional (*52, 53*); the 6-31G(d) basis set (*54*) is used for carbon and hydrogen and Los Alamos National Lab (LANL2DZ) basis set (*72, 73*) and effective core potentials for gold atoms (*74*). A convergence threshold on the density matrix of 10^{-6} and 10^{-8} for the root mean square and maximum density matrix error between iterations is used, respectively. To calculate the Current-Voltage curves for the graphene ribbons, we use a program developed by our group called GENIP (*42, 75, 76*). This program is a combination of density functional and Green's function theories, the combined formalisms consider the discrete states of the molecular systems and the continuous electronic states of the gold contacts.

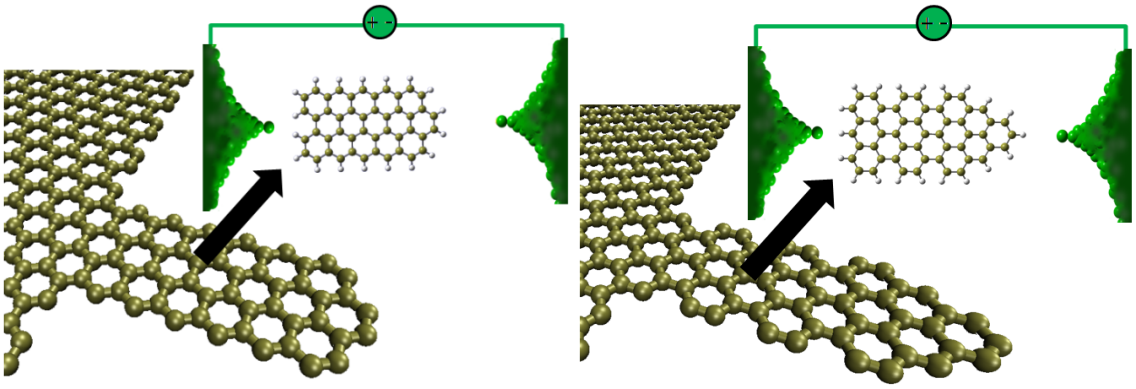

(A) (B)

Fig. 13. (**A**) Zigzag and (**B**) armchair graphene ribbons with their models used for MD simulations and to calculate the electrical transport.

5.3. Results

From twenty models of graphene vibronic devices, we calculate their resonant frequencies, and up to four peaks can be identified. The lowest frequency peak that is also the one with highest amplitude is associated with the fundamental vibrational mode.

Table 8 shows the dimensions and the calculated frequencies for each of the twenty vibronic devices. From these results, we can observe that the smaller the graphene ribbons the higher the resonant frequency. The higher calculated frequency is 0.2 THz, which is within the range of operation of THz technology, and is defined by the frequency range between 0.1 to 10 THz (*77*).

Table 8. Dimensions of the graphene vibronic devices and their fundamental (f_0), first (f_1), second (f_2) and third (f_3) resonant frequencies.

Width (Å)	Length (Å)	f_0 (THz)	f_1 (THz)	f_2 (THz)	f_3 (THz)
7.3	14.6	0.0586	0.1110	0.1458	0.1929
7.3	21.8	0.0421	0.1093	0.1333	0.1792
7.3	29.1	0.0238	0.0992	0.1161	0.1605
7.3	36.4	0.0158	0.0748	0.1115	0.1428
12.1	24.2	0.0323	0.1083	0.1257	0.1686
12.1	36.4	0.0155	0.0768	0.1123	0.1483
12.1	48.5	0.0093	0.0480	0.1073	0.1186
12.1	60.6	0.0060	0.0330	0.0835	0.1111
17.0	33.9	0.0202	0.0902	0.1143	0.1586
17.0	50.9	0.0094	0.0499	0.1089	0.1225
17.0	67.9	0.0049	0.0272	0.0766	0.1101
17.0	84.9	0.0036	0.0195	0.0522	0.0981
21.8	43.6	0.0113	0.0575	0.1107	0.1368
21.8	65.5	0.0055	0.0308	0.0806	0.1110
21.8	87.3	0.0033	0.0192	0.0492	0.0902
21.8	109.1	0.0022	0.0130	0.0325	0.0630
26.7	53.3	0.0088	0.0464	0.1068	0.1164
26.7	80.0	0.0037	0.0211	0.0565	0.1010
26.7	106.7	0.0021	0.0131	0.0323	0.0660
26.7	133.4	0.0013	0.0088	0.0244	0.0440

In the continuum mechanics model for resonators the fundamental resonant frequency f_0 is defined as (*16*):

$$f_0 = A\left(E/\rho\right)^{1/2} t/L^2 \tag{37}$$

where E is the Young's modulus, ρ is the mass density, A is the clamping coefficient, and t and L are the thickness and the length of the graphene ribbon respectively. Fig. 14A shows the values of the fundamental resonant frequency (f_0) for the twenty graphene ribbons modeled in this work, and also the curve for the continuum mechanics (CM) model. For the continuum mechanics model the Young's modulus has a value of 1 TPa (*7*). For the density we consider the density of graphite, which is 2200 kg/m^3 and for the thickness we consider the van der Waals diameter for carbon, which is 3.4 Å. The clamping coefficient "*A*" in our case is 0.028; this value will vary in experiments depending on the material in which the graphene is clamped, in our case the clamping is modeled as a row of fixed atoms in the border of the large graphene sheet.

From Fig. 14A, we can see that there is a good agreement between the values obtained by the MD simulations and the values calculated from continuum mechanics. For lengths higher than 30 Å, the 1st resonant frequency (f_1) have a similar trend than f_0 and f_1 is approximate 5 times the values of f_0 ($f_1 \approx 5f_0$), as shown in the curve in Fig. 14B. For the case of the 2nd and 3rd resonant frequencies (f_2 and f_3), we can see in Fig. 14C and Fig. 14D that it does not follow a similar trend as f_0. They follow an almost linear trend from which we can make a linear regression and extract empirical relations: $f_2 = -0.0011L + 0.155$ and $f_3 = -0.0012L + 0.193$ (f_i in THz and L in Å), with R-squared values of 0.96 and 0.95, respectively. We suggest that the reduction in the values of f_1 for small graphene ribbons and the linear trend for f_2 and f_3 could be attributed to the coupling of the vibrational modes between the large graphene sheet and the ribbons.

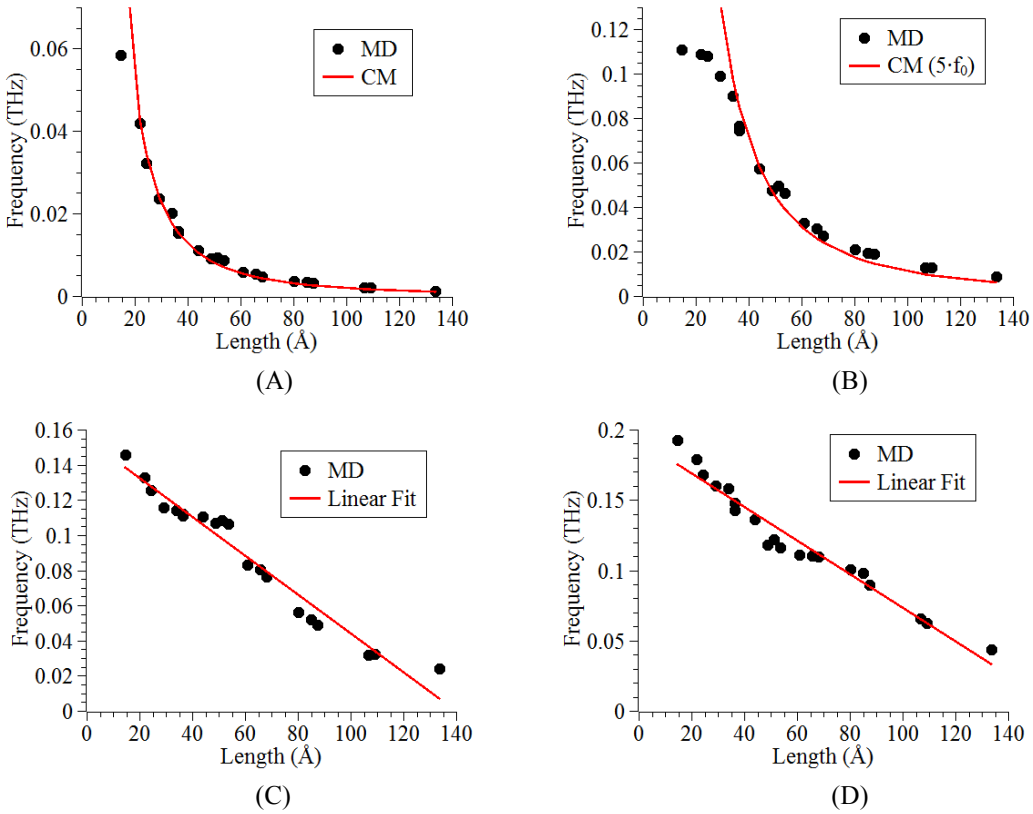

Fig. 14. Frequency vs length for **(A)** f_0, **(B)** f_1, **(C)** f_2 and **(D)** f_3 as well as the comparison with CM for **(A)** f_0 and **(B)** f_1 and linear regression for **(C)** f_2 and **(D)** f_3.

To test the use of these graphene ribbons as a molecular sensor, we simulate the interaction between one ribbon with water and IPA molecules. The graphene ribbon used for the test is 17.0 Å wide and 50.9 Å long. To test the sensitivity of this graphene vibronic device to the presence of molecules in its environment, we measure the change in the fundamental vibrational frequency to a group of water and IPA molecules. Fig. 15 shows the fundamental frequency as function of number of water and IPA molecules interacting with the graphene ribbon as well as the frequency value when the ribbon is alone. We can see that for both molecules there is a complete different trend; while for water the frequency increases as the number of water molecules in contact with the

vibronic devices increases, for IPA the frequency decreases as the number of IPA molecules increases.

We suggest that this phenomenon is due to the chemical characteristics of each molecule. For the case of water, we have a polar solvent that has a very strong attractive attraction between water molecules (Coulombic and vdW) and it has a heat of vaporization of 2.27 MJ/kg. A water molecule when is in contact with the graphene it sticks to the surface and does not evaporate, this strong interaction between the water molecule and the graphene is reflected in the large change in resonant frequency. As the number of water molecules increases, some of the water molecules evaporate and the contact time between water and graphene is reduced; the water molecules prefer the interaction with other water molecules than with the graphene surface. This is reflected in an increase in the resonant frequency as the number of water molecules increases. In case of the water, we can see that the vdW interactions play a major role in determining the change of resonant frequency in the vibronic device increasing considerably the sensitivity of the molecular sensor. The change in frequency due to the change of mass for presence of water in the resonator, as classic NEMS operate, is around 0.007 GHz for one water molecule, we can see that is negligible compare to the change in frequency due to the vdW interactions.

For the case of IPA, we have a non-polar solvent where the attractive interaction between IPA molecules is mostly due to vdW interactions and it has a heat of vaporization of 0.66 MJ/kg, which is much lower than the one of water. The IPA molecules do not stick to the graphene surface as water molecules do, but they interact

for short periods of time while behaving as vapor and there is not a preferred interaction between IPA molecules as was the case with water molecules. In this case, the change in frequency is due to the vdW interactions and the change of mass in the vibronic device; however the effects of the vdW becomes stronger than the effect of the mass as the number of molecules increases; for example, the change in frequency due to mass with one IPA molecule is approximately 0.02 GHz and the total change is 0.06 GHz, and the change in frequency due to mass for 8 IPA molecules is around 0.18 GHz and the total change is 0.56 GHz.

With the analysis of these two types of molecules, we can see that a graphene vibronic device, as the one described, is a very sensitive molecular sensor that can detect not only single molecules but can also distinguish the type of molecule that is sensing. However, more studies are needed to study how other molecules will affect and change the resonant frequencies in small graphene ribbons.

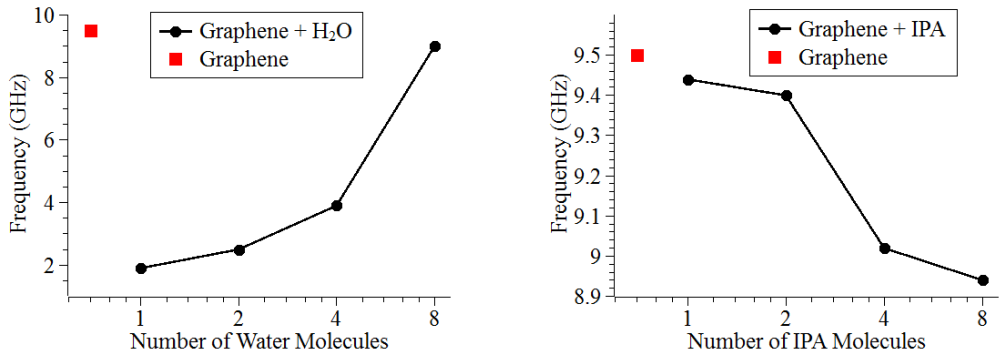

Fig. 15. Frequency versus number of (**A**) water and (**B**) IPA molecules. The red square represents the frequency of the graphene vibronic sensor when there are not molecules in contact.

We calculate the electrical transport through the graphene vibronic device as this vibrates. This vibration is represented by a change in the angle between the plane of the graphene ribbon and the line in which the gold electrodes are contained. Two types of graphene ribbons are considered in this study; one with zigzag borders and another with armchair borders.

For the case of the armchair, the model is 19.2 Å wide and 7.3 Å long (Fig. 13B). This structure only optimized for the triplet spin multiplicity. Fig. 16 shows the current-voltage curves for the armchair ribbon, as we can see; there is a rectifier behavior for the angles 0°, 15° and 45°. We suggest that this behavior is produced by the shape of the ribbon where the polarization of the ribbon under positive potential is more favorable than under negative potential promoting an "easier" transport of electrons in one direction. Another way to explain this behavior is analyzing the HOMO-LUMO or Energy gap of the device at several voltages. As shown in Fig. 16B, for angles 0°, 15° and 45° the energy gap is smaller in the positive potential region than for the other angles, being the smallest gap in this region at 45°; this is reflected in the high current at this angle. In this type of devices, two main features determine the conductivity of the device: one is the probability of tunneling from the graphene ribbon to the contact, this probability in general decreases as the angle increases; and the other is the energy gap. In case of the armchair ribbons, the energy gap plays the mayor role in determining the conductivity of the device.

For the zigzag ribbons, we have a different behavior compared to the armchair as shown in Fig. 16C. Firstly, this structure, 7.1 Å wide and 17.2 Å long (Fig. 13A),

reaches convergence for singlet spin multiplicity. This zigzag device also presents a favorable conduction in one direction but it is not as strong as in the case of the armchair ribbon. Fig. 16D shows that the energy gap is not dramatically changed when the voltage is applied. Also we can see a monotonic decrease of the energy gap as the angle between the graphene ribbon and the contacts increases; however, this does not determine the conductivity of the device. What determines the electrical properties of this vibronic device is the decrease in the probability of tunneling as the angle increases as seen in Fig. 16C the higher the angle the lower the current through the device.

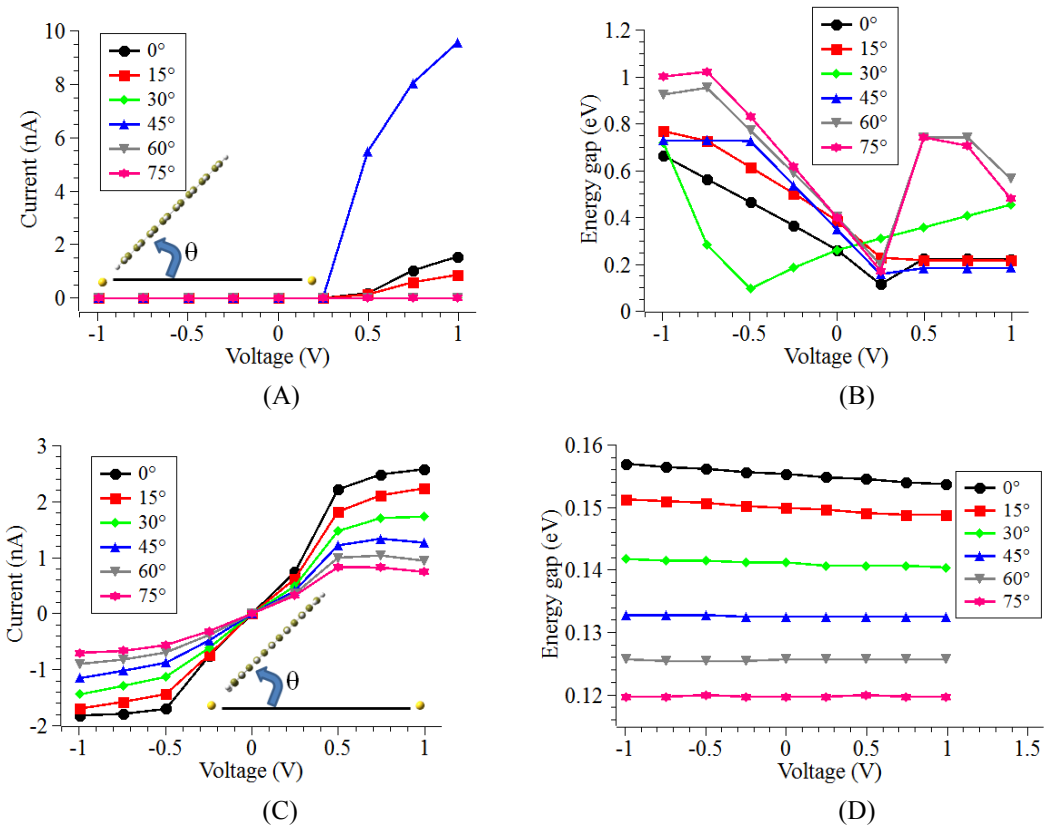

Fig. 16. Current-Voltage curves of the (**A**) armchair and (**C**) zigzag graphene vibronic device. HOMO-LUMO or Energy gap as a function of applied voltage of the (**B**) armchair and (**D**) zigzag graphene vibronic device.

The zigzag vibronic device has the characteristic that at a given voltage the current in the device is proportional to the angle between the plane of the graphene ribbon and the one of the electrodes, which is at the same time proportional to the amplitude of the oscillation. This characteristic of the zigzag device can be utilize for many purposes; for example, to read information that has been transported through a graphene sheet as an encoded vibrational signal, also to read the changes in frequency in the graphene vibronic molecular sensor in a simpler more compact way than the use of optical detection, and another application of this device can be the generation of THz electrical signals using the intrinsic vibrational modes of the graphene ribbon. To test the use of the graphene ribbon as a THz generator, we combine the MD simulations with the electrical transport calculations of the zigzag ribbon. Fig. 17A shows the current as a function of angle at 1 V for the zigzag device, as well as a fitting from where we obtain an empiric linear relation between angle and current. From that relation, we can calculate how the current will change when the graphene ribbon vibrates due to thermal excitation. Fig. 17B shows the oscillation amplitude and the current versus time, in this zigzag vibronic device the resonant frequencies of the mechanical oscillation are f_1=0.043 THz, f_2=0.107 THz, f_3=0.129 THz and f_4=0.167 THz, and the corresponding resonant frequencies of the electrical oscillations are f_1=0.08 THz, f_2=0.21 THz, f_3=0.26 THz and f_4=0.33 THz, which are within the range of operation of THz technology.

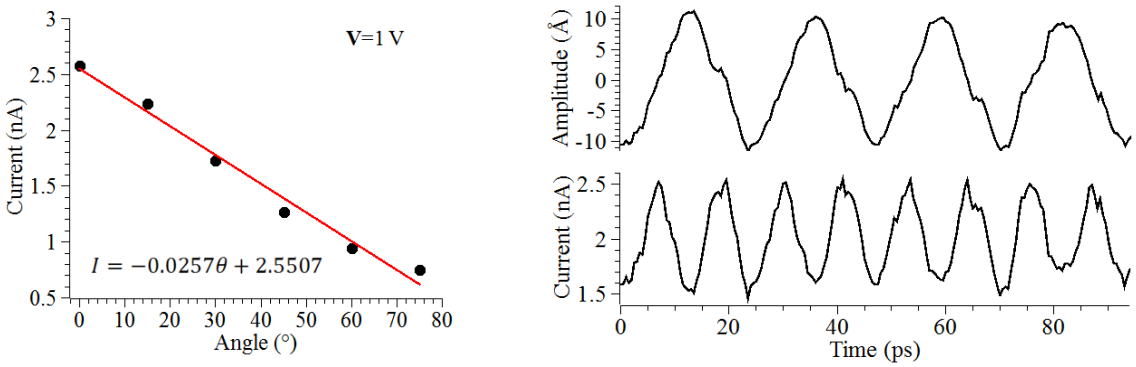

(A) (B)

Fig. 17. (**A**) Current versus angle for a zigzag virbronic device at 1V. (**B**) Amplitude and current versus time of a zigzag vibronic THz generator.

5.4. Conclusions

We simulated the natural thermal vibration of several graphene ribbons and calculated their resonant frequencies. We found that there is a good agreement between our molecular dynamics simulations and continuum mechanics models in the calculation of the fundamental resonant frequency. We also found that for the 1st resonant frequency the continuum model only works for graphene ribbons with lengths higher than 30 Å and does not work for 2nd and 3rd resonant frequencies, for which we calculated empirical linear relations of frequency with the ribbon length. We demonstrated the use of the graphene ribbons as vibronic molecular sensor with very high sensitivity that can recognize the type of molecule they are sensing depending on their van der Waals interaction and the chemical properties of the molecule. This type of sensor has potential to form a new generation of molecular spectrometers that do not only detect a molecule for their mass but also for their chemistry. Finally, using a zigzag graphene vibronic device, we demonstrate the generation of THz electrical signals using its intrinsic vibrational modes reaching frequencies of 0.3 THz. In summary, we

demonstrate the variety of applications of graphene vibronic devices that can be utilized in many fields in technology and science.

CHAPTER VI

CONCLUSIONS

This work proposed and studied two new fabrication methods that will allow not only the patterning of graphene structures, but also the formation of 1D, 2D and 3D graphene structures, as well as the control of their electronic properties by defect formation. We have also proposed and studied new graphene based devices that form part of a novel scenario called vibronics, which can be complementary to traditional electronics as demonstrated in this work.

In the carbon ion bombardment of graphene simulations, we observed four types of interactions: reflection, adsorption, transmission and vacancy formation. Reflection is dominant at energies below 10 eV. Between 10 and 100eV, adsorption is dominant and adatoms defects are formed. Between 100 eV and 100 keV, the dominant process is transmission; and above 30 eV, vacancy formation takes place being a low rate process with a constant rate of 0.14 at energies above 10keV. Single vacancies and double vacancies are observed, and after DFT optimization the double vacancies converge into 5-8-5 defects. This work provides the analysis and physical parameters needed to develop a new top down fabrication method using carbon ion bombardment of graphene. And it showed that, with this method, it is possible to control the defect formation and build carbon structures on graphene sheets opening the possibility of large scale fabrication of graphene based devices.

As a bottom-up approach, we have studied the controlled folding of graphene structures driven by molecular interactions with water nanodroplets. It is demonstrated that the non-bonded interactions between a graphene nano-structure and SiO_2 are strong enough to prevent the folding process, also it is demonstrated that the large contact area of a defect free system of graphene supported on a layer of IPA or HMDS over SiO_2 does not allow the graphene to fold. However, when we have a defective system over a layer of IPA supported on SiO_2, the water-graphene interaction overcomes the graphene-substrate interaction promoting the folding process. When the system is supported on a hydrophobic substrate such HMDS and the correct graphene geometry with large surface area and adequate nanodroplet size is used, the folding can occur. The adequate selection of substrate, graphene geometry, and nanodroplet size allows the folding and may open the possibility of a controlled fabrication of graphene based capsules, scrolls, sandwiches and rings.

In the vibronic device scenario, we modeled the natural thermal vibration of several graphene ribbons and calculated their bending mode resonant frequencies. It is found that for the fundamental resonant frequency there is a good agreement between our molecular dynamics simulations and continuum mechanics. Also, for graphene ribbons with lengths higher than 30 Å the 1st resonant frequency behaves as predicted by the continuum model. However, does not work for 2nd and 3rd resonant frequencies; for these empirical linear relations of frequency and ribbon length were calculated. It is demonstrated, with our simulations of the interaction of a graphene vibronic device with water and isopropyl alcohol molecules, that graphene ribbons can be used as vibronic

molecular sensor with very high sensitivity. These sensor are capable of recognizing the type of molecule they are sensing depending on their van der Waals interaction and the chemical properties of the molecule. It is also demonstrated that a vibronic device can be integrated with current electronics; in this case using a zigzag graphene vibronic device, we demonstrate the generation of THz electrical signals using its intrinsic vibrational modes reaching frequencies of 0.3 THz. In general, graphene ribbons can be utilized to fabricate several types of vibronic devices such as sensors, THz generators, and devices for enconding, transfer and processing of information.

In order to implement the proposed fabrication methods and devices, more studies are required. For the case of carbon bombardment of graphene, experimental tests are required, especially at low energies (10 to 100 eV), to confirm that it is possible to build carbon structures bonded to graphene sheets. Also it is important to work in developing ion beams with small diameters, in this way better resolution and control can be achieved. For the case of the folding of graphene, more theoretical and experimental studies are required in order to define the formation parameters of carbon scrolls, rings, capsules and sandwiches in various substrates.

Finally, experimental implementation and testing of the proposed devices is required to confirm the calculated values of sensitivity for the vibronic molecular sensor and the generated frequencies for the THz generator. Theoretical studies of the transmission and encoding of information in graphene structures are required. Also for the case of the armchair vibronic device, we found unusual spin transport properties that have to be further investigated.

REFERENCES

1. S. Iijima, *Nature* **354**, 56 (1991).

2. J. Che, T. Cagin, W. A. G. Iii, *Nanotechnology* **11**, 65 (2000).

3. T. W. Ebbesen, H. J. Lezec, H. Hiura, J. W. Bennett, H. F. Ghaemi *et al.*, *Nature* **382**, 54 (1996).

4. A. Krishnan, E. Dujardin, T. W. Ebbesen, P. N. Yianilos, M. M. J. Treacy, *Physical Review B* **58**, 14013 (1998).

5. K. S. Novoselov, A. K. Geim, S. V. Morozov, D. Jiang, M. I. Katsnelson *et al.*, *Nature* **438**, 197 (2005).

6. K. S. Novoselov, A. K. Geim, S. V. Morozov, D. Jiang, Y. Zhang *et al.*, *Science* **306**, 666 (2004).

7. R. S. Ruoff, D. C. Lorents, *Carbon* **33**, 925 (1995).

8. K. I. Bolotin, K. J. Sikes, Z. Jiang, M. Klima, G. Fudenberg *et al.*, *Solid State Comm.* **146**, 351 (2008).

9. M. C. Lemme, T. J. Echtermeyer, M. Baus, H. Kurz, *IEEE Electron Device Lett.* **28**, 282 (2007).

10. Y. M. Lin, K. A. Jenkins, A. Valdes-Garcia, J. P. Small, D. B. Farmer *et al.*, *Nano Lett.* **9**, 422 (2009).

11. S. Bae, H. Kim, Y. Lee, X. F. Xu, J. S. Park *et al.*, *Nat. Nanotechnol.* **5**, 574 (2010).

12. S. Stankovich, D. A. Dikin, G. H. B. Dommett, K. M. Kohlhaas, E. J. Zimney *et al.*, *Nature* **442**, 282 (2006).

13. S. Garaj, W. Hubbard, J. A. Golovchenko, *Appl. Phys. Lett.* **97**, (2010).

14. N. Patra, B. Wang, P. Král, *Nano Lett.* **9**, 3766 (2009).

15. A. K. Naik, M. S. Hanay, W. K. Hiebert, X. L. Feng, M. L. Roukes, *Nat. Nanotechnol.* **4**, 445 (2009).

16. J. S. Bunch, A. M. van der Zande, S. S. Verbridge, I. W. Frank, D. M. Tanenbaum *et al.*, *Science* **315**, 490 (2007).

17. N. L. Rangel, J. C. Sotelo, J. M. Seminario, *J. Chem. Phys.* **131**, (2009).

18. Z. Z. Sun, Z. Yan, J. Yao, E. Beitler, Y. Zhu *et al.*, *Nature* **471**, 124 (2011).

19. L. P. Biró, P. Lambin, *Carbon* **48**, 2677 (2010).

20. L. Tapaszto, G. Dobrik, P. Lambin, L. P. Biro, *Nat. Nanotechnol.* **3**, 397 (2008).

21. G. Dobrik, L. Tapasztó, P. Nemes-Incze, P. Lambin, L. P. Biró, *physica status solidi (b)* **247**, 896 (2010).

22. Y. Chen, J. Lu, Z. X. Gao, *J. Phys. Chem. C* **111**, 1625 (2007).

23. K. Kim, Z. Lee, B. D. Malone, K. T. Chan, B. Aleman *et al.*, *Physical Review B* **83**, (2011).

24. X. Xie, L. Ju, X. Feng, Y. Sun, R. Zhou *et al.*, *Nano Lett.* **9**, 2565 (2009).

25. T. Burg, S. Manalis, *Appl. Phys. Lett.* **83**, 2698 (2003).

26. M. D. LaHaye, O. Buu, B. Camarota, K. C. Schwab, *Science* **304**, 74 (2004).

27. A. Naik, O. Buu, M. D. LaHaye, A. D. Armour, A. A. Clerk *et al.*, *Nature* **443**, 193 (2006).

28. L. M. Yan, Y. F. Ma, J. M. Seminario, *J. Nanosci. Nanotechnol.* **6**, 675 (2006).

29. J. A. Seminario, L. M. Yan, Y. F. Ma, *IEEE Trans. Nanotechnol.* **5**, 436 (2006).

30. L. Miao, J. M. Seminario, *J. Phys. Chem. C* **111**, 8366 (2007).

31. J. Tersoff, *Physical Review B* **37**, 6991 (1988).

32. J. Tersoff, *Physical Review B* **39**, 5566 (1989).

33. J. Tersoff, *Phys. Rev. Lett.* **61**, 2879 (1988).

34. J. Tersoff, *Physical Review B* **38**, 9902 (1988).

35. J. F. Ziegler, J. P. Biersack, U. Littmark, *Stopping and Ranges of Ions in Matter*. (Pergamon Press, Morrisville, NC, 1985), vol. 1.

36. A. D. MacKerell, D. Bashford, Bellott, R. L. Dunbrack, J. D. Evanseck *et al.*, *J. Phys. Chem. B* **102**, 3586 (1998).

37. A. Ito, H. Nakamura, A. Takayama, *J. Phys. Soc. Jpn.* **77**, (2008).

38. O. Lehtinen, J. Kotakoski, A. V. Krasheninnikov, A. Tolvanen, K. Nordlund *et al.*, *Physical Review B* **81**, (2010).

39. P. Hohenberg, W. Kohn, *Physical Review* **136**, B864 (1964).

40. W. Kohn, L. J. Sham, *Physical Review* **140**, A1133 (1965).

41. A. Szabo, N. S. Ostlund, *Modern Quantum Chemistry: Introduction to Advanced Electronic Structure Theory*. (Dover Publications, Mineola, NY, 1996).

42. P. A. Derosa, J. M. Seminario, *J. Phys. Chem. B* **105**, 471 (2001).

43. S. Datta, *Electronic Transport in Mesoscopic Systems*. (Cambridge University Press, Cambridge U.K., 1995).

44. W. Tian, S. Datta, S. Hong, R. Reifenberger, J. I. Henderson *et al.*, *J. Chem. Phys.* **109**, 2874 (1998).

45. X. Wang, X. Li, L. Zhang, Y. Yoon, P. K. Weber *et al.*, *Science* **324**, 768 (2009).

46. J. Lahiri, Y. Lin, P. Bozkurt, I. I. Oleynik, M. Batzill, *Nat. Nanotechnol.* **5**, 326 (2010).

47. L. Tapaszto, G. Dobrik, P. Nemes-Incze, G. Vertesy, P. Lambin *et al.*, *Physical Review B* **78**, (2008).

48. S. Neubeck, F. Freitag, R. Yang, K. S. Novoselov, *Phys. Status Solidi B-Basic Solid State Phys.* **247**, 2904 (2010).

49. S. Plimpton, *J. Comput. Phys.* **117**, 1 (1995).

50. H. J. C. Berendsen, J. P. M. Postma, W. F. van Gunsteren, A. DiNola, J. R. Haak, *J. Chem. Phys.* **81**, 3684 (1984).

51. J. A. Floro, S. M. Rossnagel, R. S. Robinson, *J. Vac. Sci. Technol., A* **1**, 1398 (1983).

52. J. P. Perdew, Y. Wang, *Physical Review B* **45**, 13244 (1992).

53. J. P. Perdew, J. A. Chevary, S. H. Vosko, K. A. Jackson, M. R. Pederson *et al.*, *Physical Review B* **46**, 6671 (1992).

54. P. C. Hariharan, J. A. Pople, *Chemical Physics Letters* **16**, 217 (1972).

55. A. Hashimoto, K. Suenaga, A. Gloter, K. Urita, S. Iijima, *Nature* **430**, 870 (2004).

56. Y. Chen, J. Lu, Z. Gao, *J. Phys. Chem. C* **111**, 1625 (2007).

57. E. R. Cruz-Chu, A. Aksimentiev, K. Schulten, *J. Phys. Chem. B* **110**, 21497 (2006).

58. P. E. M. Lopes, V. Murashov, M. Tazi, E. Demchuk, A. D. MacKerell, *J. Phys. Chem. B* **110**, 2782 (2006).

59. I. J. Chen, D. Yin, A. D. MacKerell, *J. Comput. Chem.* **23**, 199 (2002).

60. J. M. Seminario, *Int J Quantum Chem* **60**, 1271 (1996).

61. L. H. Reyes, J. M. Seminario, *J. Mol. Struct.: THEOCHEM* **818**, 125 (2007).

62. E. J. Bautista, J. M. Seminario, *Int J Quantum Chem* **108**, 180 (2008).

63. L. Martínez, R. Andrade, E. G. Birgin, J. M. Martínez, *J. Comput. Chem.* **30**, 2157 (2009).

64. W. Shinoda, M. Shiga, M. Mikami, *Physical Review B* **69**, 134103 (2004).

65. J. C. Meyer, A. K. Geim, M. I. Katsnelson, K. S. Novoselov, T. J. Booth *et al.*, *Nature* **446**, 60 (2007).

66. A. L. Vazquez de Parga, F. Calleja, B. Borca, M. C. G. Passeggi, J. J. Hinarejos *et al.*, *Phys. Rev. Lett.* **100**, 056807 (2008).

67. M. Ishigami, J. H. Chen, W. G. Cullen, M. S. Fuhrer, E. D. Williams, *Nano Lett.* **7**, 1643 (2007).

68. S. Johansson, J. A. Schweitz, K. P. D. Lagerlof, *J. Am. Ceram. Soc.* **72**, 1136 (1989).

69. U. Staufer, T. Akiyama, M. R. Gullo, A. Han, R. Imer *et al.*, *Microelectron. Eng.* **84**, 1681 (2007).

70. E. P. Bellido, J. M. Seminario, *J. Phys. Chem. C* **114**, 22472 (2010).

71. M. J. Frisch, G. W. Trucks, H. B. Schlegel, G. E. Scuseria, M. A. Robb *et al.* (Gaussian, Inc., Wallingford CT, 2009).

72. W. Wadt, P. Hay, *J. Chem. Phys.* **82**, 284 (1985).

73. P. J. Hay, W. R. Wadt, *Ab initio effective core potentials for molecular calculations. Potentials for K to Au including the outermost core orbitals*. (AIP, 1985), vol. 82, pp. 299-310.

74. J. M. Seminario, J. M. Tour, *Int J Quantum Chem* **65**, 749 (1997).

75. J. M. Seminario, A. G. Zacarias, P. A. Derosa, *J. Chem. Phys.* **116**, 1671 (2002).

76. J. M. Seminario, C. De La Cruz, P. A. Derosa, L. M. Yan, *J. Phys. Chem. B* **108**, 17879 (2004).

77. B. Ferguson, X.-C. Zhang, *Nature Materials* **1**, 26 (2002).

VITA

Edson Pazur Bellido Sosa received his Bachelor of Science degree in Engineering Physics from Universidad Nacional de Ingeniería at Lima-Peru in 2007. He entered the Materials Science and Engineering program at Texas A&M University in September 2009 and received his Master of Science degree in December 2011. His research interests include quantum mechanics, condensed matter physics, nanotechnology and molecular electronics.

Mr. Bellido may be reached at The Molecular Electronics and Nanotechnology group, Department of Chemical Engineering, Texas A&M University, College Station, TX 77840-3122. His email is edsonbellido@gmail.com.